https://doi.org/10.5194/egusphere-2026-4032
Preprint. Discussion started: 28 August 2026

The contribution of the surface temperature inversion to Antarctic warming

Ben Tyler [1], Anaïs Orsi [1,2], Cécile Davrinche [3], and Charles Amory [4]

[1]Department of Earth, Ocean and Atmospheric Sciences, The University of British Columbia, Vancouver, BC, Canada
[2]Laboratoire des Sciences du Climat et de l'Environnement, LSCE-IPSL, CEA, CNRS, UVSQ, UMR8212, Université Paris-Saclay, Gif-sur-Yvette, France
[3]Université Catholique de Louvain, Louvain-la-Neuve, Belgium
[4]Institut des Géosciences de l'Environnement, CNRS/UGA/IRD/G-INP, Grenoble, France

Correspondence: Ben Tyler (contact@bentyler.ca) and Anaïs Orsi (aorsi@eoas.ubc.ca)

Abstract. Antarctica is expected to warm faster than the global average throughout the 21st century in a phenomenon called Antarctic amplification. The polar atmosphere is unique in having a strong and persistent surface temperature inversion layer, and its changing properties can dramatically affect polar warming. In this work, we reveal mechanisms behind Antarctic amplification by quantifying the contribution of this surface temperature inversion to the region's near-surface warming. Global climate models often miss the vertical resolution and physical processes needed to correctly simulate the intense near-surface inversion. Here, we downscale four global climate models with the regional climate model MAR (Modèle Atmosphérique Régional) to decompose the Antarctic near-surface potential temperature into the background potential temperature and the surface temperature inversion strength. From the late 20th to the late 21st century, we attribute 72 % of July near-surface warming over the Antarctic continent and sea ice to large-scale background warming under the Shared Socioeconomic Pathway SSP5-8.5. However, the spatial variability in this warming is driven by surface processes through their weakening of the surface temperature inversion, which explains the remaining 28 % of warming. Over the ocean, this weakening is well predicted by sea ice loss, and accounts for 41 % of the near-surface warming. By contrast, the weakening of the inversion explains 16 % of near-surface warming on the continent, where it is correlated with stronger present-day atmospheric stability, which suggests that the lapse-rate feedback contributes significantly to spatial variability in warming. The particularly strong contribution of sea ice loss to the weakening of the inversion could explain the asymmetry between Arctic and Antarctic amplification. Variability in the inversion strength could also account for discrepancies between paleoclimate proxy records.

1 Introduction

Under anthropogenic climate change, the polar surface is expected to warm more rapidly than lower latitudes and the worldwide average in a phenomenon called polar amplification (Smith et al., 2019). This amplification is expected to be asymmetric, with greater amplification in the Arctic compared to the Antarctic (Manabe and Stouffer, 1980; Salzmann, 2017; Goosse et al., 2018; Stuecker et al., 2018; Cai et al., 2021; Hahn et al., 2021). Numerous physical mechanisms cause polar amplification. For instance, it is commonly attributed to the surface albedo feedback. This occurs due to the loss of high-albedo surfaces, like ice and snow, which increases solar radiation absorption at the polar surface (e.g., Budyko, 1969; Manabe and Wetherald, 1975; Manabe and Stouffer, 1980; Holland and Bitz, 2003; Hall, 2004; Graversen et al., 2014; Dai et al., 2019). Additionally, colder regions require more warming to shed enough radiation to counteract radiative forcing. This mechanism is called the Planck feedback (Wetherald and Manabe, 1988; Langen et al., 2012; Feldl and Roe, 2013; Pithan and Mauritsen, 2014; Henry and Merlis, 2019). Polar regions also experience a positive lapse-rate feedback due to strong stable stratification in the lower atmosphere. This restricts warming to the near-surface atmosphere and causes the upper troposphere to warm less than the lower troposphere, which suppresses outgoing longwave radiation and thereby increases surface warming (Manabe and Wetherald, 1975; Cai and Lu, 2007; Graversen et al., 2014; Pithan and Mauritsen, 2014; Feldl et al., 2020; Linke et al., 2023). Increases in atmospheric heat transport towards the poles with global warming are also expected to contribute to polar amplification (Flannery, 1984; Alexeev et al., 2005; Lu and Cai, 2010; Graversen and Langen, 2019). Greater poleward oceanic heat transport may contribute as well (Holland and Bitz, 2003; Hwang et al., 2011; Salzmann, 2017; Singh et al., 2017; Shu et al., 2022). In terms of importance, the surface albedo and lapse-rate feedbacks are considered to be the dominant mechanisms driving Antarctic amplification, while atmospheric heat transport and the Planck feedback contribute substantially as well (Taylor et al., 2013; Graversen et al., 2014; Pithan and Mauritsen, 2014; Goosse et al., 2018; Cai et al., 2021; Hahn et al., 2021).

Another unique feature of polar regions is the persistent surface temperature inversion in their near-surface atmosphere. A surface temperature inversion refers to temperature increasing with altitude above the land or ocean surface (Zhang et al., 2011). This phenomenon is widespread throughout Antarctica because the cold polar surface's outgoing radiation generally exceeds incoming radiation (Phillpot and Zillman, 1970). Surface temperature inversions have been frequently identified and studied over the Antarctic continent, especially over the cold Antarctic Plateau (e.g., Phillpot and Zillman, 1970; Riordan, 1977; Connolley, 1996; Hudson and Brandt, 2005; Pietroni et al., 2014; Baas et al., 2019; Yang et al., 2025). The inversion is particularly strong over the plateau and ice shelves while decreasing in strength towards the coast (Phillpot and Zillman, 1970; Connolley, 1996). Inversions are present over sea ice surrounding Antarctica as well (Andreas et al., 2000; Pavelsky et al., 2011). Seasonally, in the Antarctic interior, winter inversions are particularly strong and can be virtually permanent (Phillpot and Zillman, 1970; Connolley, 1996). For instance, at Antarctic Plateau sites, the inversion is maintained throughout the winter and is still common during summer (Pietroni et al., 2014; Yang et al., 2025). Connolley (1996) measured an average wintertime inversion strength of more than 25 °C over the Antarctic interior, quantified as the difference between 1.5 m temperature and the maximum temperature within the troposphere. Importantly, the presence of a cold inversion layer promotes stable stratification within the boundary layer (Bintanja et al., 2011). This amplifies surface warming by inhibiting vertical mixing, which prevents the surface warming signal from being diluted by upward propagation in the atmosphere. This trapping effect then amplifies warming via the lapse-rate feedback (Bintanja et al., 2012; Feldl et al., 2020). Throughout this study, we expect stronger stable stratification in the lower atmosphere to be associated with greater near-surface Antarctic warming according to the lapse-rate feedback.

The change of the surface temperature inversion in polar regions has important implications for paleoclimate proxies. Some proxies depend on surface temperature and therefore the surface inversion, while others depend on the temperature higher up in the atmosphere. For example, borehole temperatures used to reconstruct past temperatures are related to Antarctic surface

https://doi.org/10.5194/egusphere-2026-4032
Preprint. Discussion started: 28 August 2026

temperature (Buizert et al., 2021). Certain temperature reconstruction techniques using gas stable isotopes (e.g., with δ^{15}N) or using the difference between ice-trapped gas age and the surrounding ice's age similarly depend on surface temperature (Bender et al., 2006; Buizert et al., 2021; Servettaz et al., 2023). By contrast, water stable isotope reconstructions (e.g., using δ^{18}O and δD) do not approximate surface temperatures but rather the temperature of precipitation formation, or the condensation temperature, which occurs higher in the atmosphere (Jouzel and Merlivat, 1984; van Lipzig et al., 2002; Helsen et al., 2005). This vertical separation could introduce discrepancies between proxy records (Buizert et al., 2021; Servettaz et al., 2023).

Simulating the surface temperature inversion in polar regions can be difficult. For instance, in Arctic regions, CMIP6 global climate models (GCMs) often overestimate inversion strength during winter (Hahn et al., 2021). To improve confidence in simulating the Antarctic atmospheric boundary layer in this analysis, we dynamically downscale the GCMs we study using the Modèle Atmosphérique Régional (MAR), which is a regional climate model (RCM) specializing in polar regions. MAR improves the horizontal resolution as well as the vertical resolution in the lower atmosphere to better simulate features like topographic and boundary-layer gradients (Davrinche et al., 2025). Additionally, its physical processes are adapted to polar regions, such as its representations of surface snow density, roughness length, cloud microphysics, and turbulence (Gallée, 1995; Agosta et al., 2019; Amory et al., 2021). MAR has been shown to reliably simulate Antarctic climate. For example, MAR reduces GCM biases in Antarctic near-surface wind speed when used to downscale the four GCMs used in this study (Davrinche et al., 2025), and it successfully represents Antarctica's surface mass balance (Agosta et al., 2019). Gilbert et al. (2026) find that an ensemble of RCMs, including MAR, is better at simulating Antarctic near-surface conditions than ERA5 reanalysis data. These results show benefits of using MAR to model Antarctic boundary layer conditions.

The goal of this study is to characterize the contribution of the inversion layer to Antarctic warming and amplification. To accomplish this, we simulate the Antarctic boundary layer in four CMIP6 GCMs dynamically downscaled using MAR. This allows us to quantify the proportion of projected 21$^{\text{st}}$-century Antarctic near-surface warming that is caused by the change in the strength of the surface temperature inversion under the Shared Socioeconomic Pathway SSP5-8.5. Additionally, we characterize the relationship between the Antarctic surface temperature inversion and two processes which could drive warming by weakening the inversion strength: stable stratification over the Antarctic continent and sea ice loss in the surrounding ocean. Understanding how the inversion strength changes over time has important implications for explaining discrepancies between paleoclimate proxy records of temperature and clarifying the drivers of polar amplification in Antarctica.

2 Methods

2.1 Climate simulations

To study how the surface temperature inversion contributes to Antarctic warming and amplification, we use data from Davrinche et al. (2025), who dynamically downscaled simulations from four GCMs using MAR. All four GCMs participated in CMIP6, the most recent Coupled Model Intercomparison Project (Eyring et al., 2016). Our study area is a 6125 km × 5145 km rectangle. It extends from 90° S to approximately 55° S in latitude at its northernmost points in its corners, thus encompassing the entire Antarctic continent and a sizeable portion of the surrounding ocean.

https://doi.org/10.5194/egusphere-2026-4032
Preprint. Discussion started: 28 August 2026

Table 1. Description of selected GCMs based on Table 2 from Davrinche et al. (2025). Information includes model name, institution of origin, horizontal resolution (Williams et al., 2024), and global equilibrium climate sensitivity (ECS) (Flynn and Mauritsen, 2020). SIC_i represents mean July sea ice concentration (SIC) averaged across all grid cells south of 60° S from 1980–2000. SIC_f represents the same measurement for 2080–2100. ΔSIC represents the difference between the mean July 1980–2000 SIC and the mean July 2080–2100 SIC in each grid cell, averaged across the same region. The SIC data are from each GCM before downscaling.

Model	Institution	Resolution (km)	ECS	SIC_i (%)	SIC_f (%)	ΔSIC (%)
UKESM1-0-LL	MOHC/NERC/NIMS-KMA/NIWA	250	5.31	62	29	−34
IPSL-CM6A-LR	IPSL	250	4.50	72	44	−28
CNRM-CM6-1	CNRM-CERFACS	250	4.81	61	18	−43
MPI-ESM1-2-HR	MPI-M/DWD DKRZ	100	2.84	44	27	−17

2.1.1 CMIP6 global climate models

This study uses data from four CMIP6 GCMs: UKESM1-0-LL (Sellar et al., 2019), IPSL-CM6A-LR (Boucher et al., 2020), CNRM-CM6-1 (Voldoire et al., 2019), and MPI-ESM1-2-HR (Mauritsen et al., 2019). Throughout this study, we refer to these models as UKESM, IPSL, CNRM, and MPI, respectively. These models were originally chosen due to their effective simulation of polar climate (Davrinche et al., 2025). Additionally, they simulate a variety of equilibrium climate sensitivity (ECS) values for the planet. For instance, UKESM has a particularly high ECS while MPI has a weak ECS (Table 1). The models also show different trends in 21$^{\mathrm{st}}$-century sea ice loss, from high sea ice loss reported by CNRM to low sea ice loss reported by MPI (Table 1).

2.1.2 Regional downscaling

The GCM simulations are dynamically downscaled using the regional climate model MAR, a hydrostatic polar-oriented model (Gallée and Schayes, 1994; Gallée, 1995) that is well suited for the study of Antarctic climate (Agosta et al., 2019; Amory et al., 2021; Davrinche et al., 2024). This study uses MAR v3.11 and the model setup is described in Kittel et al. (2021) and Davrinche et al. (2024). In the horizontal, MAR uses the standard Antarctic polar stereographic grid at 35 km resolution (EPSG:3031). The resulting study area is a grid of 176 by 148 cells. In the vertical, MAR uses 24 hybrid levels extending from approximately 2 m above the surface to about 16 km, with eight levels below 100 m. Throughout this study, we consider the lowest σ level (about 2 m) as the near-surface level. The simulations have fixed topography from Bedmap2, which also provides the ice and rock masks (Fretwell et al., 2013).

To downscale each GCM, MAR's boundaries are forced with climatological data from the GCMs at 6 h intervals and outputs are generated at 3 h intervals. The decomposition of potential temperature (Sect. 2.2.1) is then calculated using the 3 h data, but throughout this study, we use monthly averages of all data. Nudging is applied from the model top down to approximately 500 hPa (level 16), leaving the lower 15 levels free to evolve according to the model physics. The top of the atmosphere in

https://doi.org/10.5194/egusphere-2026-4032
Preprint. Discussion started: 28 August 2026

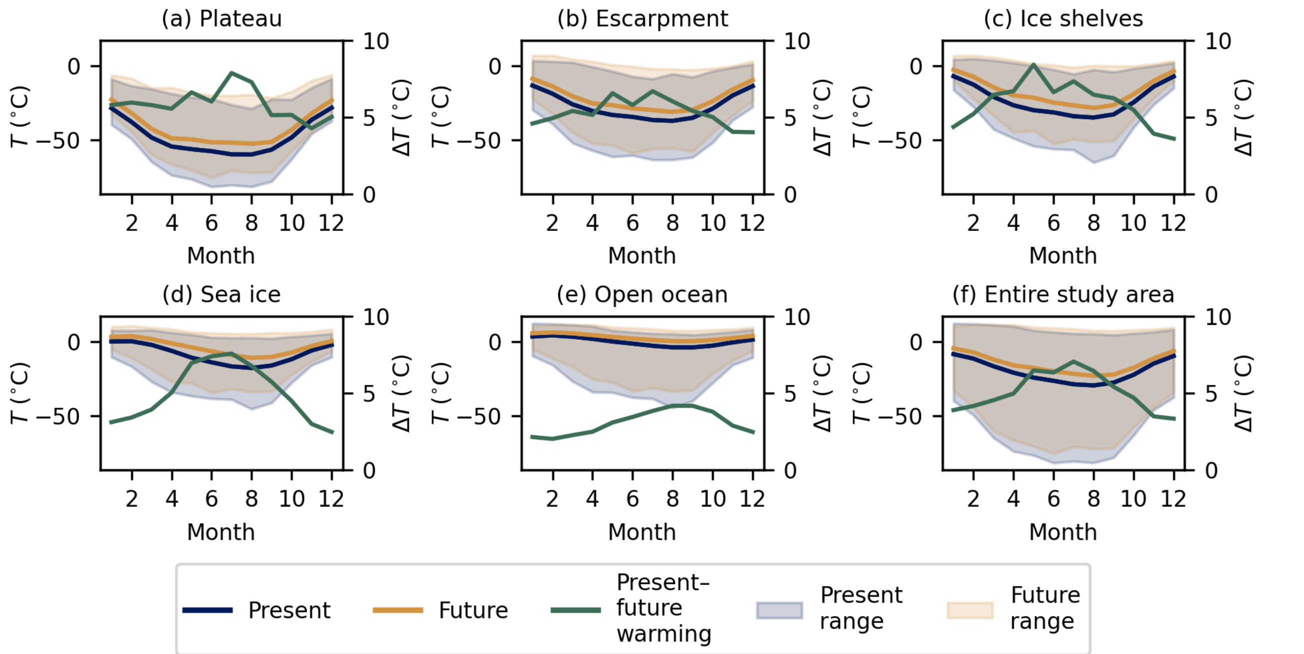

Figure 1. In winter, Antarctic near-surface temperature is coldest, and Antarctic warming peaks. The subplots show mean monthly near-surface temperature (T) during 1980–2000 (labelled as "Present") and 2080–2100 (labelled as "Future") alongside the change in near-surface temperature from present to future (ΔT) by study region. Data are reported for IPSL before downscaling under SSP5-8.5, and are regridded to this study's 35 km grid using bilinear interpolation. Ranges represent the minimum and maximum temperature in any grid cell.

MAR is forced with temperature and wind above about 10 km while its lateral edges are forced with pressure, temperature, wind components, and specific humidity. It is also forced with sea ice concentration and sea surface temperature at the ocean–atmosphere interface. MAR is forced with one member from each GCM (r1i1p1f1 for IPSL and MPI, and r1i1p1f2 for UKESM and CNRM). For more information, Davrinche et al. (2025) offer the original description of the downscaling procedure. All non-downscaled GCM data in this study come from publicly available CMIP6 multi-model output (Sect. S7). When referring to a downscaled GCM simulation, we use the corresponding GCM's abbreviation preceded by "MAR-" (e.g., MAR-UKESM).

2.1.3 Temporal range of simulations

Our study focuses exclusively on July because of the month's notable surface inversions and the strong warming projected in Antarctic winter. Throughout the year, Antarctic monthly mean near-surface temperature ranges from approximately $-18\,°\mathrm{C}$ to $0\,°\mathrm{C}$ over sea ice and from $-47\,°\mathrm{C}$ to $-20\,°\mathrm{C}$ over the continent during the 1980–2000 period in IPSL prior to downscaling. The temperature reaches its minimum in approximately July and August (Fig. 1). Accordingly, temperature inversions in Antarctica are generally strongest during the winter (Connolley, 1996). At the same time, near-surface warming in and around Antarctica is expected to peak in austral winter with climate change (Fig. 1). This trend aligns with recent research showing

https://doi.org/10.5194/egusphere-2026-4032
Preprint. Discussion started: 28 August 2026

that CMIP6 models project greater Antarctic warming in winter compared to summer with future anthropogenic emissions (Cai et al., 2021) and that Antarctic warming peaks in winter after quadrupling atmospheric CO_2 (Hahn et al., 2021). As a result, since we are studying the inversion layer's role in warming, we focus on the month of July when warming is high and the surface inversion is strong and well defined.

To characterize Antarctic warming and amplification throughout the 21st century, we analyze model outputs from two 21-year time periods as in Bracegirdle et al. (2020). The first time period is 1980–2000, which we call the "present-day" period, and the second is 2080–2100, which we call the "future" period. Section S1.1 and Table S1 explain additional details about data availability in each period. Throughout this study, a variable symbol preceded by the Δ symbol represents the mean value of that variable averaged across July 2080–2100 minus the mean value of that variable averaged across July 1980–2000. We refer to this calculation as the "21st-century change" in the variable.

We conduct the simulations under the SSP5-8.5 emissions scenario. This is the highest emissions scenario run by the Intergovernmental Panel on Climate Change (IPCC) and it represents a worldwide radiative forcing of $8.5\,\mathrm{W\,m^{-2}}$ by 2100, and average global warming of $4.8\,°\mathrm{C}$ by the end of the 21st century compared to 1850–1900 (IPCC, 2023). When comparing non-downscaled CMIP6 data to the MAR runs, we use data from the CMIP6 historical and SSP5-8.5 experiments (Eyring et al., 2016; O'Neill et al., 2016).

2.2 Climate variables

2.2.1 Potential temperature and potential temperature deficit

To study near-surface warming, we analyze potential temperature (θ) at the lowest σ level in our simulations, which is about $2\,\mathrm{m}$ above the surface. Potential temperature is conserved when air undergoes adiabatic changes in elevation. This renders it helpful for comparing temperature between different locations in Antarctica given that the continent has large elevation gradients. Using the procedure from Davrinche et al. (2024) based on van den Broeke and van Lipzig (2003), we separate near-surface θ into the background potential temperature (θ_0) and the potential temperature deficit (D_θ), where $\theta = \theta_0 + D_\theta$ (D_θ is the same as Δ_θ in Davrinche et al. (2024)). θ_0 is calculated by linearizing the free atmosphere's potential temperature profile then extrapolating it downward. D_θ represents the deviation of θ from θ_0 near the surface and must always be non-positive. We describe the potential temperature decomposition in further detail in Appendix A. Since radiation loss from the Antarctic surface causes surface temperature inversions resulting in persistent near-surface temperature deficits (Phillpot and Zillman, 1970; van den Broeke and van Lipzig, 2003), we interpret the temperature deviation term D_θ as the inversion strength, following Bintanja et al. (2014). This definition is useful over Antarctica because calculating the inversion strength as the temperature difference between the surface and a certain pressure level (e.g., Ruman et al., 2022) is complicated by the continent's large elevation gradients.

https://doi.org/10.5194/egusphere-2026-4032
Preprint. Discussion started: 28 August 2026

2.2.2 Sea ice concentration

Over the ocean, the four GCMs simulate sea ice concentration (SIC), which is a boundary condition for MAR. SIC represents the percentage of a grid cell covered in sea ice. At high SIC values, our data contain artefacts in SIC measurements because the maximum SIC threshold in MAR is 95 %.

2.2.3 Static stability

We measure atmospheric stability using the squared Brunt–Väisälä frequency (N^2). This is calculated as $N^2 = \frac{g}{\theta}\frac{\partial \theta}{\partial z}$, where g is the acceleration due to gravity and z is altitude. Positive N^2 represents statically stable conditions and negative N^2 represents statically unstable conditions. Following Stull (2017), we approximate N^2 as

$$N^2 = \frac{g}{\overline{\theta}} \frac{\theta_8 - \theta_1}{z_8 - z_1} \tag{1}$$

where θ_1 and θ_8 are the potential temperatures at the first and eighth σ layers above the surface, z_1 and z_8 are the heights of the first and eighth σ layers above the surface, and $\overline{\theta} = \frac{\theta_1 + \theta_8}{2}$. The first σ layer is about $2\,\mathrm{m}$ above the surface and the eighth σ layer is about $100\,\mathrm{m}$ above the surface. By approximating N^2 up to the eighth layer, we aim to characterize the static stability throughout the lower atmosphere. Figure S1 shows that our estimates of N^2 are not sensitive to the choice of the top atmospheric layer (Sect. S1.2).

2.2.4 Turbulent kinetic energy

Turbulent kinetic energy (TKE) represents the kinetic energy contained within turbulent atmospheric motions, calculated per unit mass (Stull, 1988; Holtslag, 2015). Given that greater TKE represents more energy contained in turbulent motions, we interpret TKE as a proxy for turbulent mixing. Since we are interested in the turbulent mixing near the surface, we quantify mixing as mean TKE from the first to the eighth σ layer above the surface, calculated as follows:

$$\overline{\mathrm{TKE}} = \frac{\int_{z_1}^{z_8} \mathrm{TKE}(z)dz}{z_8 - z_1}. \tag{2}$$

For the remainder of the study, we omit the overline symbol from $\overline{\mathrm{TKE}}$ and refer to the estimate as TKE. Figure S2 shows that our quantification of TKE is not sensitive to the choice of top atmospheric layer (Sect. S1.2).

2.2.5 Quantifying the contribution of the inversion to warming

In Sect. 3.2, we calculate the contribution of the change in the inversion strength to Antarctic warming by grid cell as follows:

$$f(\Delta\theta, \Delta\theta_0, \Delta D_\theta) = \begin{cases} \frac{\Delta D_\theta}{\Delta\theta_0} & \text{if } \Delta D_\theta < 0 \\ \frac{\Delta D_\theta}{\Delta\theta} & \text{if } \Delta D_\theta \geq 0. \end{cases} \tag{3}$$

When $\Delta D_\theta \geq 0$, its contribution to warming is simply the ratio of the change in the inversion strength to the total potential temperature change. However, when $\Delta D_\theta < 0$, the contribution of ΔD_θ to warming becomes the ratio of the change in the inversion strength to the warming that would occur without the D_θ effect (i.e., the background warming $\Delta\theta_0$).

https://doi.org/10.5194/egusphere-2026-4032
Preprint. Discussion started: 28 August 2026

Additionally, in Sect. 3.2, we calculate the polar amplification factor (PAF) as $\Delta\theta_{\mathrm{local}}/\Delta\theta_{\mathrm{global}}$ (Bintanja et al., 2012; Previdi et al., 2020). $\Delta\theta_{\mathrm{local}}$ represents the July warming at a grid cell (Swain et al., 2026). $\Delta\theta_{\mathrm{global}}$ represents the mean July 2080–2100 near-surface potential temperature minus the mean July 1980–2000 near-surface potential temperature averaged across the whole globe. $\Delta\theta_{\mathrm{global}}$ is calculated from CMIP6 temperature and pressure data for each GCM before downscaling.

2.3 Regions of study

We divide Antarctica into three regions: ice shelves, escarpment, and plateau. The ice shelves are defined as continental grid cells with less than 50 % grounded ice and maximum elevation 200 m above sea level. Selecting 200 m excludes grid cells with unreasonably high elevations. Remaining continental grid cells with a maximum elevation of 2300 m are defined as escarpment, and those with an elevation greater than 2300 m are defined as plateau. This threshold is from Davrinche et al. (2024).

In the ocean, the sea ice region represents oceanic grid cells with at least 15 % SIC in July averaged over the present-day period (Boeke et al., 2021). Within this region, we also define a permanent sea ice cover region (PSIC). This includes all grid cells containing over 90 % SIC in July averaged over each of the present-day and future periods. We categorize the rest of the ocean in our study area as open ocean.

2.4 Statistical analysis

2.4.1 Spatial correlation

In Sect. 3.1 and 3.4, we calculate the correlation between climatological variables across spatial regions. To perform spatial correlation analyses, we calculate Spearman's rank correlation coefficient (r_s) on grid cell data (Spearman, 1904; Haining, 1991). We chose r_s due to the presence of non-linear associations between some variables. Calculating the statistical significance of r_s values without accounting for the spatial nature of the data results in incorrect p-values due to large-scale spatial trends and positive spatial autocorrelation (Haining, 1991). To avoid this, we follow the procedure described by Haining (1991) to test the significance of r_s calculated with spatial data. In our correlations, each data point corresponds to a grid cell. First, we detrend the data with respect to continental elevation via linear regression to minimize spurious correlations between quantities that follow similar patterns with elevation (Dale and Fortin, 2014). We test each r_s value for statistical significance at the 95 % significance level by implementing a modified t-test which accounts for spatial autocorrelation by calculating an effective sample size using SpatialPack (Clifford et al., 1989; Dutilleul et al., 1993; Vallejos et al., 2020). We use Sturges' Rule to calculate the number of classes in the modified t-test (Legendre and Legendre, 2012; Vallejos et al., 2020).

2.4.2 Testing temporal trends

To test whether climatological data at each grid cell or across a whole region are significantly different between July 1980–2000 and July 2080–2100, we group the yearly data into present-day and future categories, then we use the Kruskal–Wallis test with a 95 % significance level (Kruskal and Wallis, 1952; Davrinche et al., 2025). Within each time-period grouping, we assume that data points for individual years are independent.

https://doi.org/10.5194/egusphere-2026-4032
Preprint. Discussion started: 28 August 2026

2.5 Regression models

2.5.1 Analysis of the influence of sea ice on the surface inversion

We fit a quadratic regression model to the present-day July SIC and D_θ grid cell data over the ocean from each downscaled GCM simulation. The models are in the form $D_\theta = a\cdot\mathrm{SIC}^2+b\cdot\mathrm{SIC}+c$, and each data point used in training a model represents the mean July values of D_θ and SIC averaged over 1980–2000 at a grid cell. We then use these regression models to predict mean D_θ per grid cell for July 2080–2100 solely from SIC data. To do this, we calculate $\Delta D_\theta = 2a\cdot\Delta\mathrm{SIC}\cdot\mathrm{SIC}_i+a\cdot(\Delta\mathrm{SIC})^2+b\cdot\Delta\mathrm{SIC}$ where $\Delta\mathrm{SIC}=\mathrm{SIC}_f-\mathrm{SIC}_i$. SIC_i represents mean July 1980–2000 SIC and SIC_f represents mean July 2080–2100 SIC per grid cell. Therefore, we can predict the mean July D_θ for 2080–2100 at each grid cell as $D_{\theta,f} = D_{\theta,i}+\Delta D_\theta$ where the subscripts i and f have the same meanings as above. We set all positive predicted $D_{\theta,f}$ values to $0\,\mathrm{K}$, since $D_\theta > 0\,\mathrm{K}$ cannot occur according to the variable's definition. The selection of the prediction regions for both the present-day quadratic regressions and the predictions of future D_θ are explained in the Supplement (Sect. S1.3).

2.5.2 Analysis of the influence of static stability on the surface inversion

Similarly, for each downscaled GCM, we fit a linear regression model to the mean present-day N^2 and ΔD_θ grid cell data by continental region to assess how well present-day static stability predicts the change in the surface temperature inversion. Over the ice shelf region, a small number of coastal grid cells strongly skew the regressions due to their unusually high ΔD_θ values. This appears to be driven by high warming occurring over the ocean, which we later attribute to sea ice loss (Sect. 3.3). Therefore, we only train our ice shelf regression models on grid cells in the Ronne and Ross Ice Shelves. We further limit the prediction grid cells to cells with ΔD_θ values under 4.1 K, which removes any anomalously high values of ΔD_θ remaining.

2.5.3 Model evaluation

We quantify the success of the present-day SIC–D_θ regression models using mean absolute error (MAE) and mean absolute percentage error (MAPE). To quantify the success of these models at predicting future D_θ, we calculate their MAE and MAPE with respect to their corresponding downscaled GCM outputs for July 2080–2100. We quantify the success of our N^2–ΔD_θ regression models using MAE and median absolute error. MAPE is not useful for these regressions because some grid cells have very low magnitudes of ΔD_θ which could yield extremely high absolute percentage error values.

We perform spatial cross-validation when calculating these performance metrics to assess the predictive ability of our models on unknown data (Sun et al., 2023). We use the scikit-learn KMeans algorithm to divide the ice shelf region into six distinct clusters and the plateau, escarpment, and sea ice regions into five clusters each (Pedregosa et al., 2011). Our cross-validation and block selection procedures are further explained in the Supplement (Sect. S1.4). We perform spatial cross-validation instead of random cross-validation because spatial autocorrelation causes random cross-validations to underestimate model error when predicting hidden testing data (Roberts et al., 2017).

https://doi.org/10.5194/egusphere-2026-4032
Preprint. Discussion started: 28 August 2026

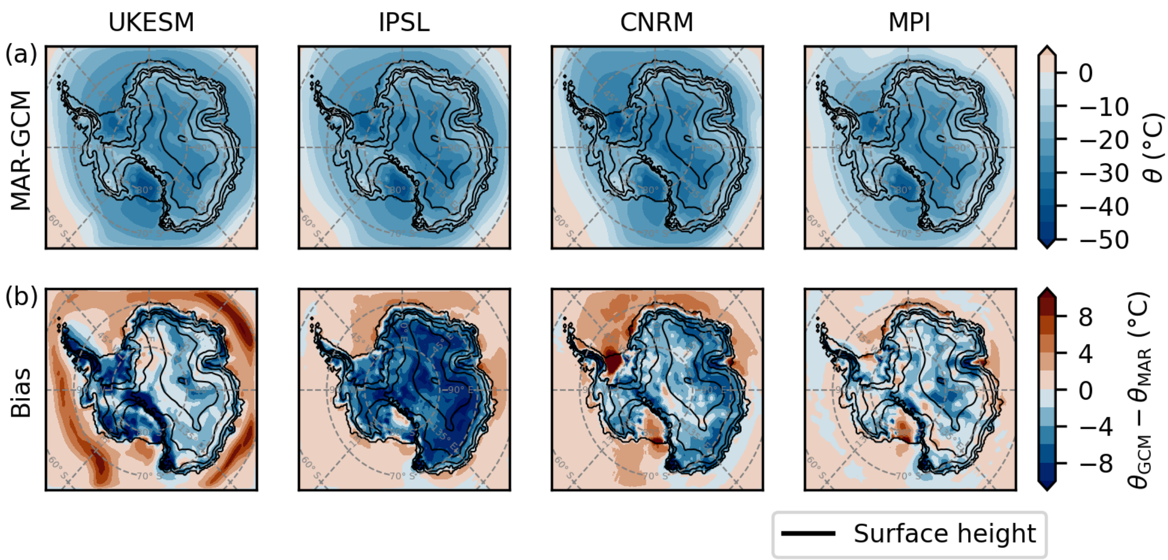

Figure 2. Near-surface July potential temperature (θ) climatology in Antarctica and the surrounding ocean, averaged over 1980–2000. (a) Potential temperature downscaled by MAR and (b) non-downscaled potential temperature (θ_{GCM}) minus downscaled potential temperature (θ_{MAR}).

3 Results

3.1 Spatial patterns in Antarctic boundary layer variables

First, we report the spatial patterns of several climate variables that are important to our analysis. Figure 2a shows that θ is coldest over the ice shelves and plateau but warmer on the steep escarpment. Over the ocean, θ increases with greater distance from the continent. Figure 2b depicts the bias in θ in CMIP6 compared to the corresponding MAR simulations, indicating that these CMIP6 models overestimate θ in the Southern Ocean and underestimate θ on the Antarctic continent compared to MAR. The θ pattern in Fig. 2a aligns well with the presence of sea ice, shown in Fig. 3a. From July 1980–2000 to 2080–2100, there is a ring of high sea ice loss around Antarctica in all the downscaled models (Fig. 3b). We later show the importance of this annular pattern in controlling warming and amplification (Sect. 3.3).

Our temperature decomposition shows that the July surface temperature inversion is both strong and omnipresent throughout Antarctica. On the continent, it is generally strongest over the plateau and ice shelves, while it weakens over the steeper escarpment region (Fig. 4, 5). Over the sea ice, the inversion decays gradually with increasing distance from the continent. Past the edges of the sea ice, the inversion becomes very weak over the open ocean (Fig. 4).

https://doi.org/10.5194/egusphere-2026-4032
Preprint. Discussion started: 28 August 2026

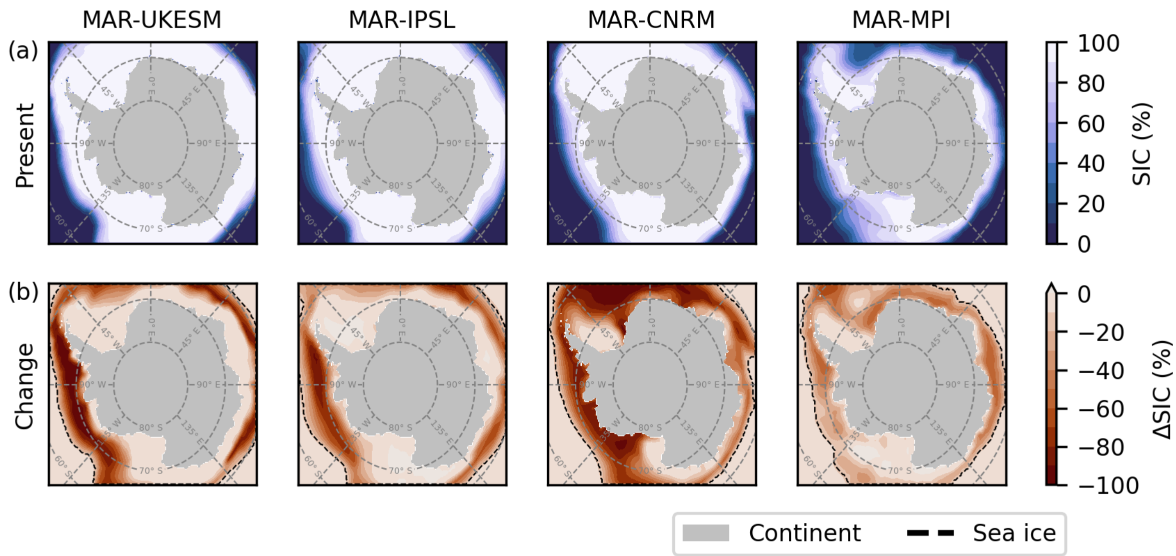

Figure 3. Sea ice concentration (SIC) climatology by downscaled GCM simulation. (a) Mean July SIC for 1980–2000, and (b) change in mean July SIC between 1980–2000 and 2080–2100 (ΔSIC). In (b), the sea ice contour indicates the northernmost sea ice edge position for a threshold of 15 % SIC.

3.1.1 Spatial patterns of the surface inversion over the continent

Spatially, stronger inversions are associated with higher N^2 and lower TKE over the continent (Fig. 4, 5). D_θ, N^2, and TKE are particularly well correlated over the ice shelves, where the pairwise r_s values between the three variables range in magnitude from 0.84 to 0.89 in the multi-model mean (Table 2). The variables are also strongly associated over the plateau with multi-model mean r_s magnitudes of 0.68 to 0.76. They are more weakly correlated over the escarpment with multi-model mean r_s magnitudes of 0.39 to 0.68, but the correlations remain significant across all regions and models when reporting the correlations for each individual downscaled simulation (Table S2). This aligns with the ability of surface inversions to increase atmospheric stability and reduce turbulent mixing, as explained in the Introduction. The two transects we plot in Fig. 5 also show how stronger inversions are associated with stronger stability and weaker turbulent mixing. However, TKE is not entirely controlled by stratification: It is also strongly correlated with near-surface wind speed given that the multi-model mean r_s between these two variables ranges from 0.93 to 0.95 among regions (Table 2). Higher wind speeds are known to promote mechanical turbulence. Strong winds disrupt the inversion layer by mixing the inversion's cold near-surface air and the warmer air above it (Pietroni et al., 2014; Yang et al., 2025). Both stratification and wind are important controls on turbulent mixing.

https://doi.org/10.5194/egusphere-2026-4032
Preprint. Discussion started: 28 August 2026

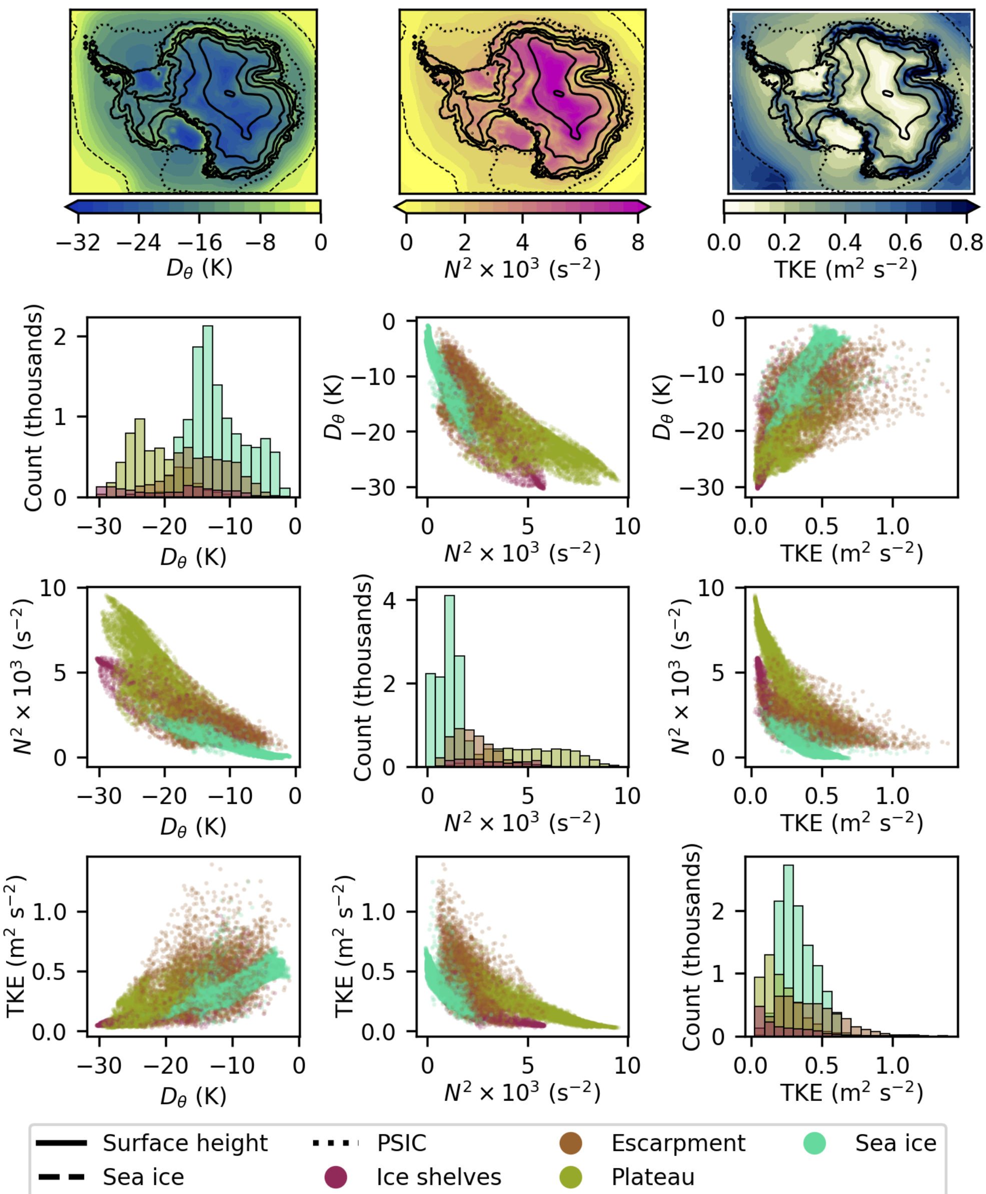

Figure 4. Climatology of the present-day inversion layer over Antarctica. Each data point is averaged across July 1980–2000 in MAR-IPSL. The top row depicts spatial patterns of the potential temperature deficit (D_θ), static stability (N^2), and turbulent kinetic energy (TKE). The sea ice contour indicates the northernmost sea ice edge position for a threshold of 15 % SIC. The diagonal subplots from the second to fourth row show the distribution of grid cell values for each variable by region. The remaining subplots depict bivariate relationships for grid cell data by region. Please see Fig. S3–S5 for the other downscaled GCMs.

https://doi.org/10.5194/egusphere-2026-4032
Preprint. Discussion started: 28 August 2026

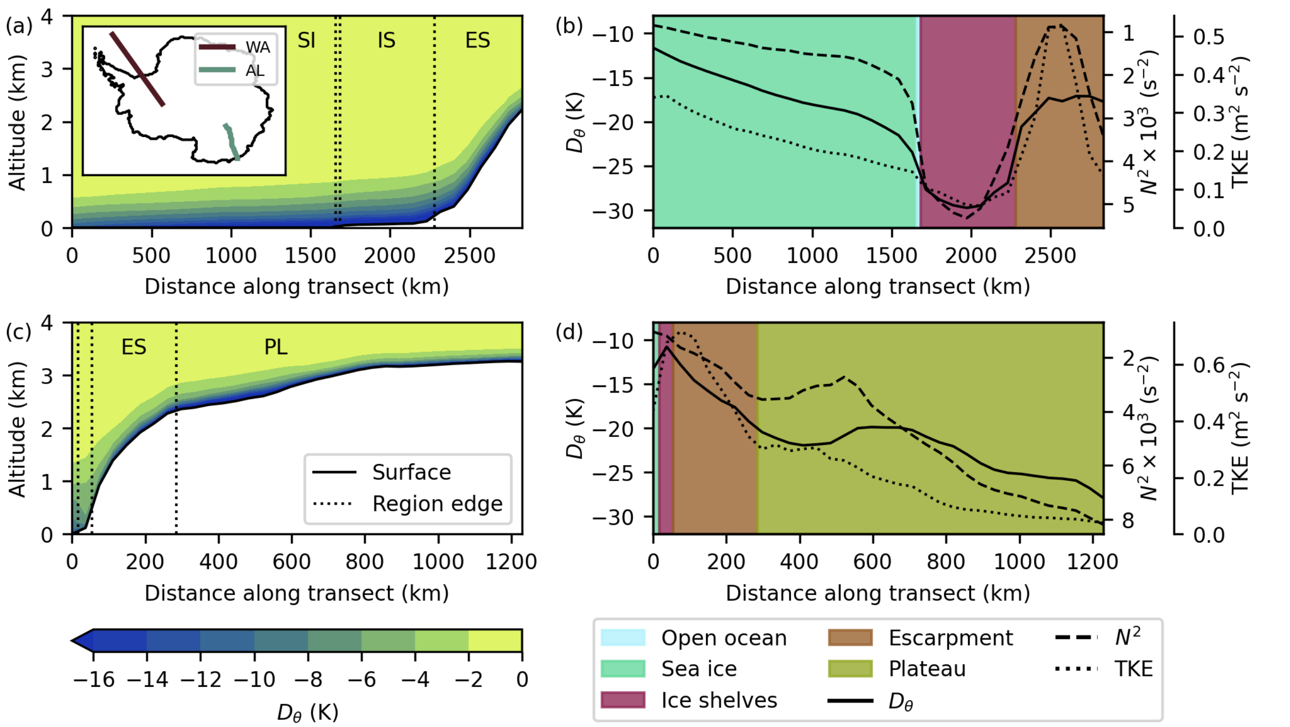

Figure 5. The covariation of inversion layer variables along two Antarctic transects. The top row shows the transect over West Antarctica and the Ronne Ice Shelf (WA), where (a) depicts the potential temperature deficit (D_θ) by altitude above sea level and (b) shows the variation of D_θ, static stability (N^2), and turbulent kinetic energy (TKE) along the transect. The bottom row shows the transect over Adélie Land (AL) from Davrinche et al. (2024), where (c) and (d) depict the same variables as the top row. SI represents sea ice, IS represents ice shelf, ES represents escarpment, and PL represents plateau. Data are from MAR-IPSL.

Table 2. Spearman's rank correlation coefficient (r_s) calculated for pairs of inversion variables by Antarctic region. D_θ is the potential temperature deficit, N^2 is static stability, TKE is turbulent kinetic energy, and WS is near-surface wind speed at the third σ level (approximately 8 m above the surface). The spatial correlations are calculated using the mean July 1980–2000 grid cell data from the downscaled GCMs. Each cell represents the multi-model mean r_s. All correlations from each downscaled GCM are statistically significant at the 95 % significance level (Table S2).

Region	D_θ–N^2	D_θ–TKE	N^2–TKE	TKE–WS
Plateau	−0.71	0.68	−0.76	0.95
Escarpment	−0.56	0.39	−0.68	0.94
Ice shelves	−0.89	0.84	−0.88	0.93

https://doi.org/10.5194/egusphere-2026-4032
Preprint. Discussion started: 28 August 2026

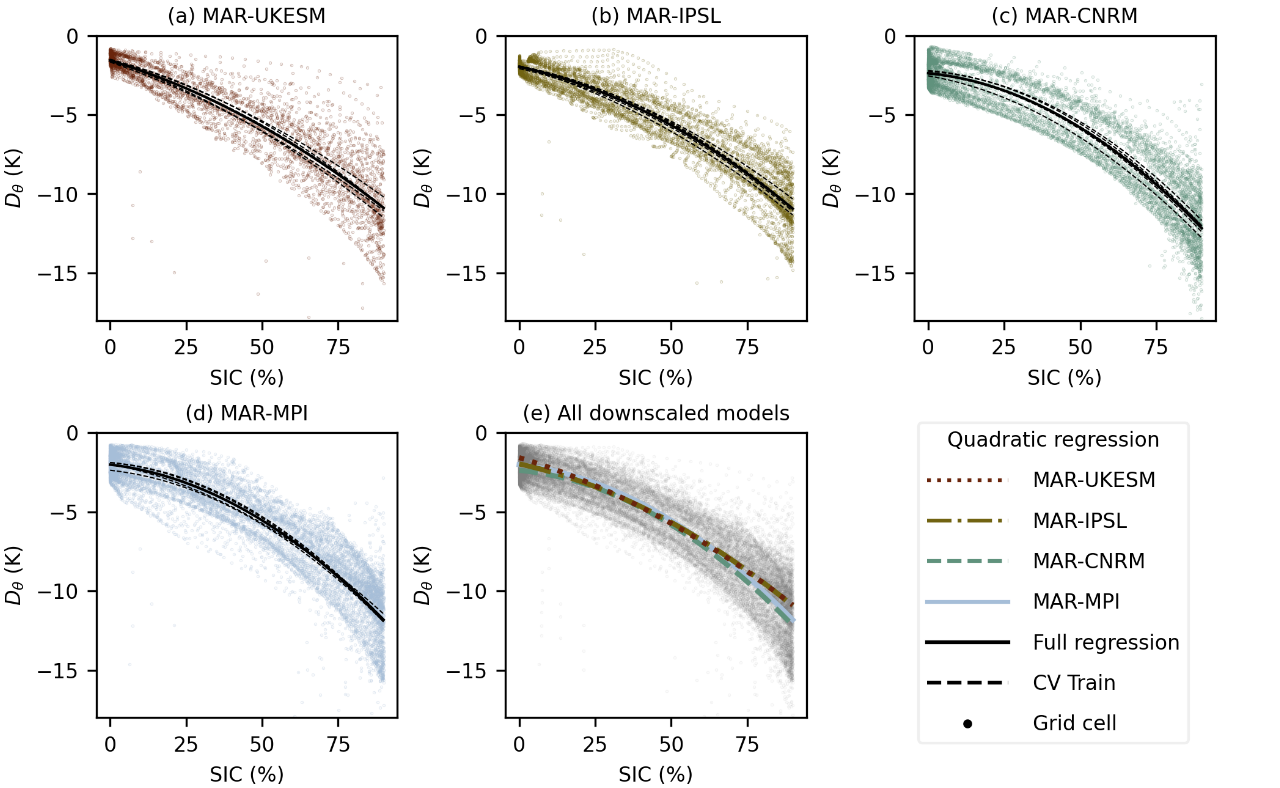

Figure 6. Greater July sea ice concentration (SIC) predicts stronger potential temperature deficit (D_θ) in the ocean surrounding Antarctica. Each data point is averaged across 1980–2000. "Full regression" represents the non-cross-validated regression calculated using all the available data while "CV Train" represents quadratic regressions generated from training data during five-fold cross-validation. Low values of D_θ are cut off to improve readability.

3.1.2 Spatial patterns of the surface inversion over the ocean

Over the sea ice, D_θ decreases in magnitude with decreasing SIC and reaches near-zero values at the edges of the sea ice region (Fig. 4). This is because exposing open ocean warms the atmosphere by raising the ocean-to-atmosphere heat flux, which destabilizes the inversion layer (Screen and Simmonds, 2010; Pavelsky et al., 2011; Rinke et al., 2013; Zhang et al., 2021). We demonstrate the strong control that SIC exerts on D_θ by fitting quadratic regression models to present-day downscaled grid cell data for SIC and D_θ. This yields a negative quadratic relationship between SIC and D_θ which is consistent across models and well replicated by cross-validation, as shown in Fig. 6 and quantified in Table S3. Our evaluation of the regression models in Table S4 shows that SIC is a reliable predictor of D_θ given the low error in the models (MAE = 1.02–1.34 K, MAPE = 23–30 %). We conclude that SIC is important in determining the spatial patterns of D_θ in the ocean around Antarctica.

https://doi.org/10.5194/egusphere-2026-4032
Preprint. Discussion started: 28 August 2026

Table 3. 21st-century warming metrics in Antarctica and the surrounding ocean. Change in potential temperature ($\Delta\theta$), change in background potential temperature ($\Delta\theta_0$), change in potential temperature deficit (ΔD_θ), the contribution of ΔD_θ to warming, and the polar amplification factor (PAF) from July 1980–2000 to July 2080–2100 averaged across each Antarctic region under SSP5-8.5. Each unbracketed value represents the multi-model mean of the downscaled GCMs and is reported with the lowest and highest downscaled GCM estimates in brackets. The regional $\Delta\theta$, $\Delta\theta_0$, and ΔD_θ averages are statistically significant at the 95 % significance level in all the listed regions across all downscaled GCMs (Table S5).

Region	$\Delta\theta$ (K)	$\Delta\theta_0$ (K)	ΔD_θ (K)	ΔD_θ contribution (%)	PAF
Plateau	6.5 [5.6, 7.9]	5.2 [4.0, 6.5]	1.3 [0.9, 1.6]	20 [14, 28]	1.4 [0.9, 1.7]
Escarpment	5.5 [4.0, 6.3]	4.9 [3.3, 5.7]	0.6 [0.5, 0.7]	11 [7, 16]	1.1 [0.9, 1.3]
Ice shelves	6.9 [4.8, 8.6]	5.3 [3.4, 6.3]	1.7 [1.2, 2.2]	23 [16, 26]	1.4 [1.2, 1.7]
Sea ice	9.1 [5.4, 12.8]	4.7 [3.2, 6.0]	4.3 [2.2, 6.8]	41 [34, 49]	1.8 [1.5, 2.6]
Continent	6.2 [4.8, 7.1]	5.1 [3.7, 6.1]	1.1 [0.9, 1.2]	16 [13, 23]	1.3 [1.0, 1.5]
Continent+sea ice	7.6 [5.1, 9.6]	4.9 [3.4, 5.7]	2.7 [1.7, 3.8]	28 [25, 32]	1.5 [1.3, 2.0]

3.2 Contribution of the change in inversion strength to Antarctic warming

This section quantifies the contribution of the change in potential temperature deficit to the total near-surface warming over the Antarctic continent and surrounding ocean. Across all downscaled models, the near-surface potential temperature warms by 7.6 [5.1, 9.6] K over the continent and sea ice (Table 3), where the bracketed numbers represent the minimum and maximum values reported among the four downscaled GCMs. There is notable spatial variability in the warming signal (Fig. 7a). It is particularly high over the sea ice compared to the continent. On the continent, the plateau and ice shelves experience high warming while the escarpment's warming appears lower (Table 3). The background potential temperature warming signal ($\Delta\theta_0$) is relatively uniform and almost entirely statistically significant in all four models (Fig. 7b). By contrast, ΔD_θ is highly variable in space (Fig. 7c). In all four models, there is a full or partial ring of statistically significant ΔD_θ over the sea ice with mean warming of 4.3 [2.2, 6.8] K (Table 3). We attribute this warming to sea ice loss in Sect. 3.3. ΔD_θ appears much lower over the continent, at 1.1 [0.9, 1.2] K (Table 3). We investigate the relationship between the lapse-rate feedback and the ΔD_θ pattern over the continent in Sect. 3.4.

We further calculated the warming contributions of background warming and the change in the inversion strength. In all models, the mean value of the warming signal is largely determined by background warming patterns ($\Delta\theta_0$). However, the spatial variability in the warming is mainly explained by the surface processes driving the spatial pattern in ΔD_θ. Over the continent, ΔD_θ explains 16 [13, 23] % of the overall near-surface warming, while over the sea ice, it explains 41 [34, 49] % of the near-surface warming (Table 3). This disproportionate influence of the inversion contribution in the ocean is depicted in Fig. 7d. This suggests that surface processes substantially amplify Antarctic near-surface warming beyond the background warming signal, especially over the sea ice.

https://doi.org/10.5194/egusphere-2026-4032
Preprint. Discussion started: 28 August 2026

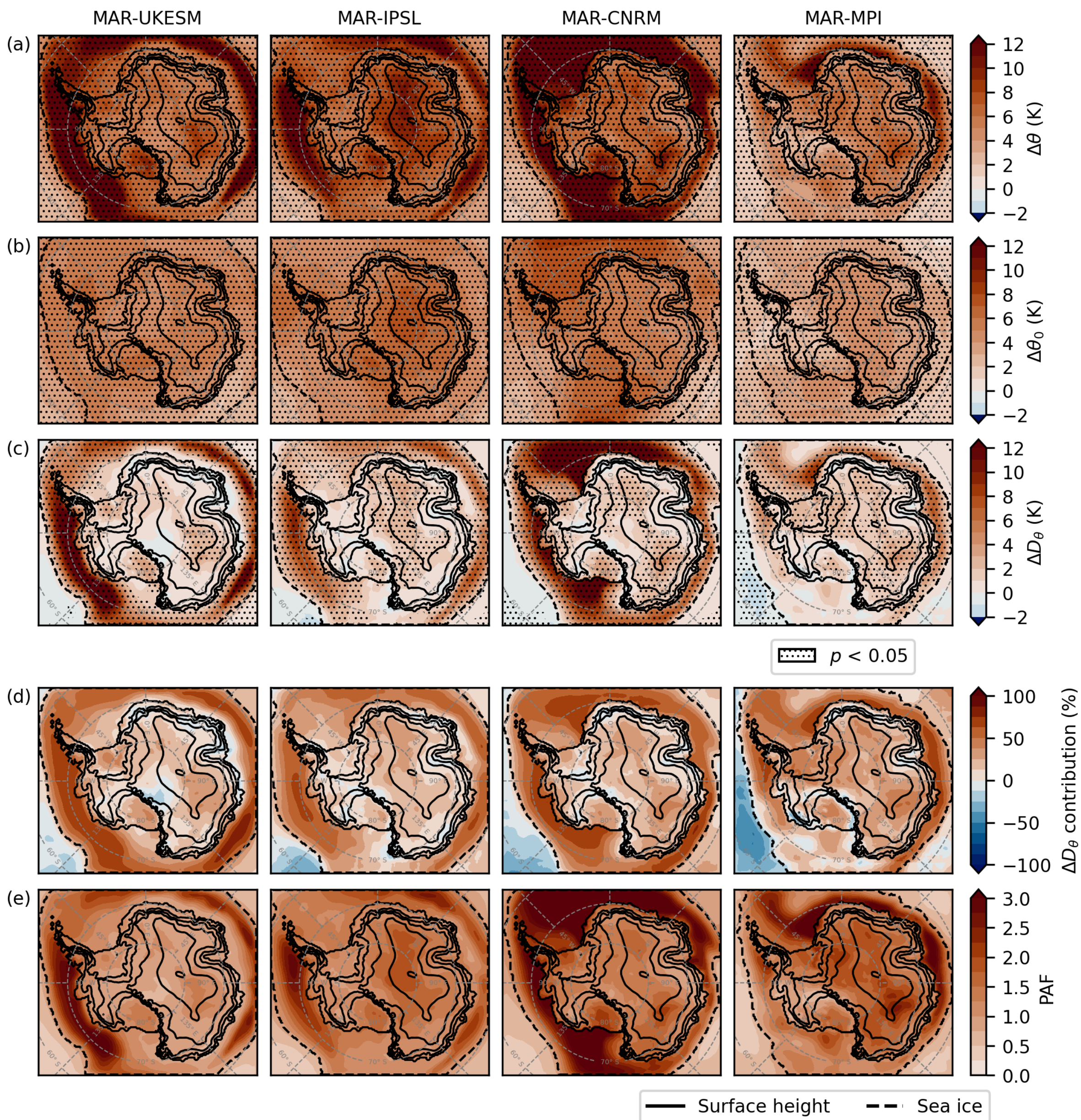

Figure 7. The surface temperature inversion drives spatial variability in near-surface Antarctic warming. (a) Change in potential temperature ($\Delta\theta$), (b) change in background potential temperature ($\Delta\theta_0$), (c) change in potential temperature deficit (ΔD_θ), (d) the contribution of ΔD_θ to warming, and (e) polar amplification factor (PAF) over the surface of Antarctica and the surrounding ocean in July from 1980–2000 to 2080–2100 under SSP5-8.5. Each column represents data from one GCM downscaled by MAR. The first three rows report statistical significance at the 95 % significance level. The sea ice contour indicates the northernmost sea ice edge position for a threshold of 15 % SIC.

https://doi.org/10.5194/egusphere-2026-4032
Preprint. Discussion started: 28 August 2026

Since ΔD_θ drives spatial variability in $\Delta\theta$, it also strongly influences spatial variation in the polar amplification signal. This is evidenced by the alignment between the spatial patterns in Fig. 7c and 7e. The amplification appears highest over the sea ice with a PAF of 1.8 [1.5, 2.6] compared to 1.3 [1.0, 1.5] over the continent because of the strong warming effect of sea ice loss (Sect. 3.3, Table 3). Over the continent, the amplification may be slightly higher over the plateau and ice shelves, where PAF is 1.4 [0.9, 1.7], than over the escarpment region, where PAF is 1.1 [0.9, 1.3] (Table 3). In summary, the large-scale background potential temperature explains 72 [68, 75] % of near-surface warming in Antarctica throughout the 21st century under SSP5-8.5 and primarily sets the magnitude of the warming. Meanwhile, changes in the inversion strength explain 28 [25, 32] % of the warming and drive spatial variability in Antarctic near-surface warming and amplification (Fig. 7, Table 3). In the following sections, we investigate possible mechanisms responsible for this variability.

3.3 Contribution of sea ice loss to near-surface warming over the ocean

In this section, we describe how sea ice loss explains the strong near-surface warming in the ocean surrounding Antarctica. In Sect. 3.1.2, we observe that SIC is a strong predictor of D_θ over the ocean as expected based on the negative relationship between ocean–atmosphere heat flux and SIC. This spatial relationship should also apply temporally as sea ice is lost and exposes more of the ocean surface to the atmosphere. Namely, our present-day quadratic regressions of D_θ versus SIC should also predict future D_θ based on the present-day and future SIC. Indeed, Fig. 8 and S6 show that ΔD_θ is well predicted qualitatively by ΔSIC and present-day SIC. Furthermore, Table S6 shows that the quadratic regression models offer reasonable first-order predictions of D_θ over the ocean in July 2080–2100 given the low model error: The multi-model mean MAE is 0.75 K and, excluding MAR-UKESM, the multi-model mean MAPE is 24 % (MAR-UKESM has an unreasonably high MAPE that is likely skewed by grid cells with low D_θ magnitudes). The satisfactory model performance is further justified by the fact that the multi-model mean future D_θ predicted by the regression models (-2.7 K after averaging across prediction regions) is close to the mean future D_θ (-3.0 K) generated by the downscaled GCMs (Table S6). These results confirm that sea ice loss is an important control on the ΔD_θ signal.

Additionally, there are consistent residuals left unexplained by the regressions (Fig. S7). We find that the quadratic models tend to overestimate the weakening of the inversion compared to the downscaled GCMs (Table S6, Fig. S6, S7). Notably, the models often underestimate the inversion strength near the Antarctic Peninsula while overestimating it off the coast of East Antarctica. This pattern might be caused by cold air draining off the PSIC and the continent near the Antarctic Peninsula (Parish and Bromwich, 1998), in particular from the Ronne Ice Shelf, which may buffer warming from sea ice loss. To conclude, sea ice loss controls the change in inversion strength over the ocean surrounding Antarctica. It is responsible for the ring of high warming and amplification off the Antarctic coast. Consequently, 21st-century Antarctic warming will be strongly affected by the future pattern of sea ice loss.

3.4 Contribution of the lapse-rate feedback to continental near-surface warming

We now turn to examine what contributes to the change in the inversion strength over the continent. The lapse-rate feedback is an important amplifier of near-surface warming in polar regions, so it may explain spatial variability in the weakening of

https://doi.org/10.5194/egusphere-2026-4032
Preprint. Discussion started: 28 August 2026

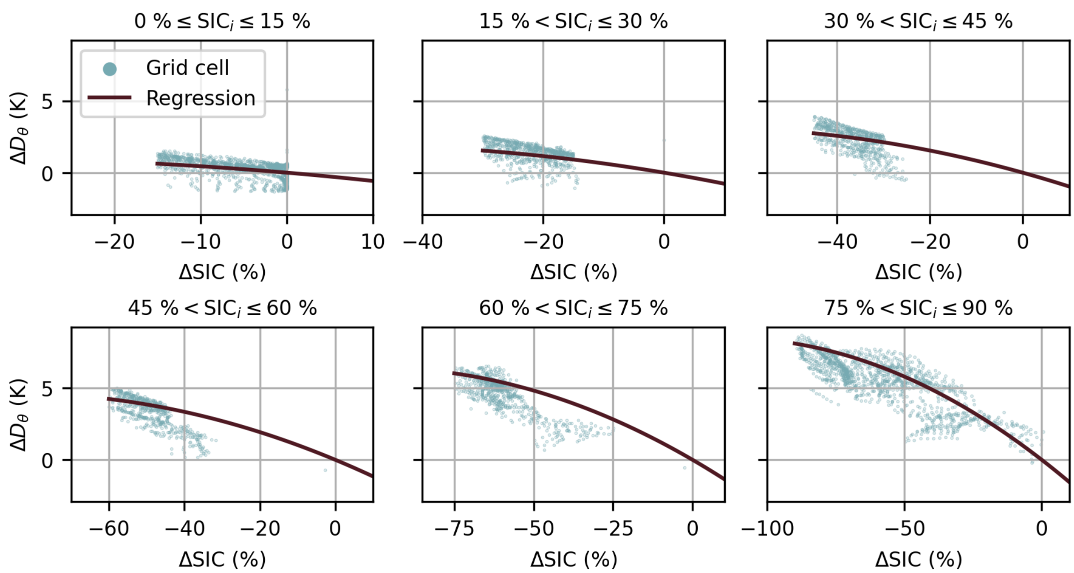

Figure 8. Predicting the 21st-century change in July inversion strength (ΔD_θ) from the change in sea ice concentration (ΔSIC) and present-day sea ice concentration (SIC$_i$). Data are shown for MAR-IPSL only (all models are shown in Fig. S6). The depicted regression model is the full regression prior to cross-validation calculated from all available data. It is derived from the present-day relationship between D_θ and SIC (Sect. 3.1.2) and is superimposed on grid cell data. In each subplot, only grid cell data with the mean July 1980–2000 SIC$_i$ values indicated above the subplot are plotted, and that subplot's predictions are calculated using the mean value of the corresponding SIC$_i$ range (e.g., SIC$_i$ $= 7.5\,\%$ is used to generate the regression predictions in the top left subplot).

the surface inversion. Consequently, we expect regions with strong inversions and therefore high near-surface static stability in the present day to show greater weakening of the surface inversion during the 21st century. Indeed, the correlation coefficients between these variables in Table 4 confirm this. In the multi-model mean, r_s between ΔD_θ and present-day D_θ ranges from -0.47 to -0.58 across the continental regions. Likewise, r_s between ΔD_θ and N^2 ranges from 0.42 to 0.45. These relationships are consistent across downscaled GCMs (Table S7).

To further characterize this relationship, we fit a linear regression model to ΔD_θ and N^2 in each region and for each downscaled GCM to assess whether stable stratification can reliably predict the weakening of the inversion. The coefficients of these regressions are shown in Table S8. Over the plateau, N^2 is successful at predicting ΔD_θ to a first order (Fig. 9a). Across the downscaled GCMs, the multi-model mean regression MAE is 0.60 K and the median absolute error is 0.56 K compared to predicted ΔD_θ values of about 0 K to 3 K. We interpret this as sufficiently low error to show that N^2 is a first-order predictor of ΔD_θ. The regressions strongly underestimate warming in Wilkes Land in MAR-UKESM, MAR-CNRM, and MAR-MPI, while they often overestimate warming close to the Ross Ice Shelf near the South Pole (Fig. S8a). Stable stratification is also a first-order predictor of ΔD_θ over the Ronne and Ross Ice Shelves (Fig. 9c). In this region's regressions, the multi-model mean MAE is 0.68 K and median absolute error is 0.63 K compared to predicted ΔD_θ values of about 0 K to 3 K. Similar

https://doi.org/10.5194/egusphere-2026-4032
Preprint. Discussion started: 28 August 2026

Table 4. Stronger inversions and greater atmospheric stability in the present day are associated with greater weakening of surface inversions. Spearman's rank correlation coefficient (r_s) is reported in the downscaled multi-model mean for the 21st-century change in inversion strength (ΔD_θ) with both the present-day inversion strength D_θ and static stability N^2. All correlations in each downscaled GCM are statistically significant at the 95 % significance level except in the plateau for MAR-UKESM (Table S7).

Region	ΔD_θ–D_θ	ΔD_θ–N^2
Plateau	−0.50	0.42
Escarpment	−0.58	0.42
Ice shelves	−0.47	0.45

to the plateau, this error is low enough to show that N^2 predicts ΔD_θ to a first order. Unlike the plateau, there are no clear consistent patterns in the regression residuals over the ice shelves (Fig. S8c). Over the escarpment, stable stratification is a poor predictor of ΔD_θ (Fig. 9b). This is clear from the multi-model mean MAE of 0.61 K and median absolute error of 0.52 K in the corresponding regressions because the error magnitude is similar to the range of ΔD_θ values predicted (about 0 to 2 K). This could be because surface inversions and stratification are generally weaker over the escarpment to begin with, so the lapse-rate feedback may not be the dominant process driving near-surface warming. The error is generally consistent between different numbers of cross-validation folds and between downscaled GCMs, although MAR-CNRM and MAR-MPI have notably high error on the ice shelves (Table S9). In conclusion, correlation and linear regression analyses indicate that the lapse-rate feedback amplifies the weakening of the inversion over the Antarctic continent. This contributes to spatial variability in near-surface warming and polar amplification beyond the mean background signal.

3.5 Inter-model variability in warming and amplification

In this section, we compare warming and amplification patterns between downscaled models. Over the ocean, there is notable inter-model variability in the local warming and amplification (Fig. 7, Table S5). The warming sensitivity to sea ice loss appears similar between models considering that the spatial D_θ sensitivity to SIC is robust across models (Fig. 6e). Instead, the variability in warming over the ocean and, in turn, the entire study area appears closely related to the magnitude of sea ice loss as ΔD_θ seems to decrease with decreasing sea ice loss (Fig. 10). For instance, the high total ΔD_θ in MAR-CNRM is clearly driven by its exceptionally high sea ice loss. The ECS values of the GCMs are not reliable predictors of their downscaled ΔD_θ and $\Delta\theta$ values, which are instead more closely related to each model's sea ice behaviour. In particular, MAR-UKESM reports lower ΔD_θ and $\Delta\theta$ than MAR-CNRM over the sea ice and continent together despite UKESM's higher global ECS (Table S5). The sea ice loss in a model also influences its polar amplification. Notably, MAR-CNRM's high total PAF is still driven by its high sea ice loss despite normalizing local warming by global warming. By contrast, despite its somewhat high total ΔD_θ, the PAF in MAR-UKESM scales with MAR-IPSL and MAR-MPI (Fig. 10). Overall, the sea ice loss pattern drives changes in the inversion strength and polar amplification.

https://doi.org/10.5194/egusphere-2026-4032
Preprint. Discussion started: 28 August 2026

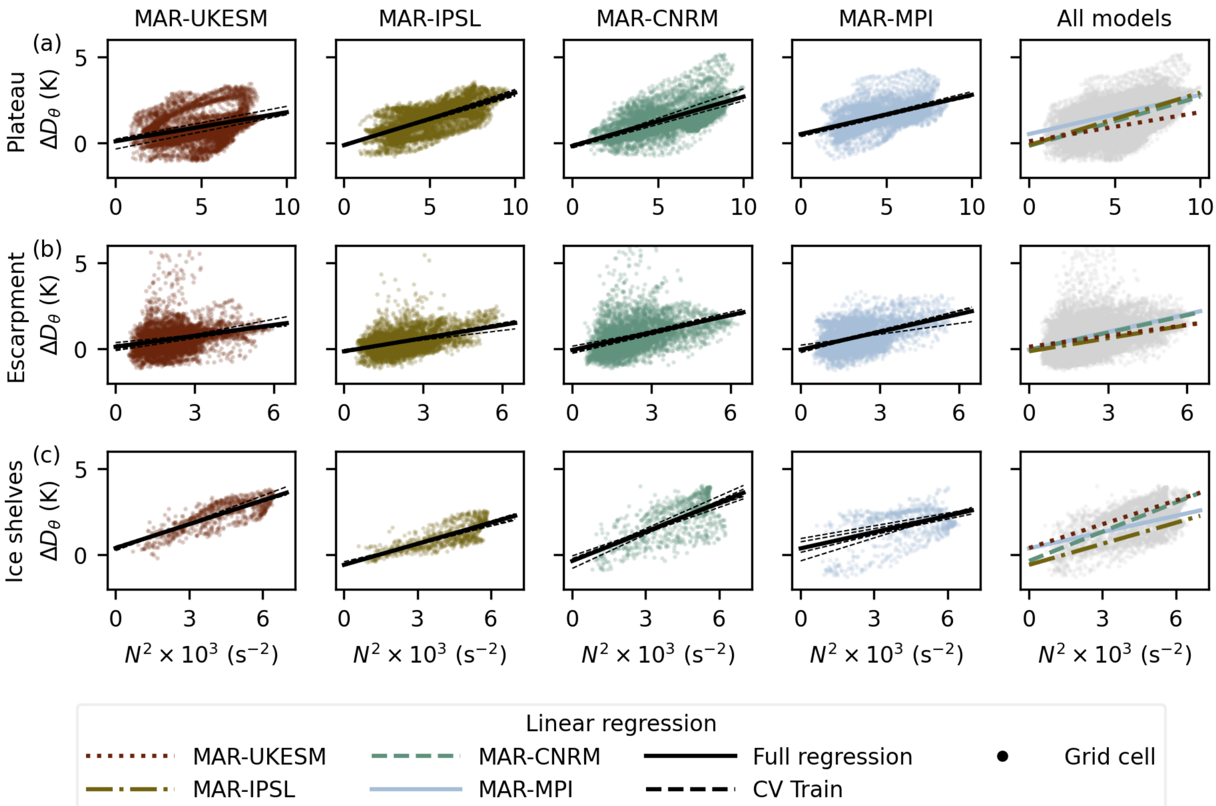

Figure 9. Predicting the 21st-century change in the July potential temperature deficit (ΔD_θ) from mean present-day July static stability (N^2). Plots depict the (a) plateau, (b) escarpment, and (c) Ronne and Ross Ice Shelves. "Full regression" represents the non-cross-validated regression calculated using all the available data while "CV Train" represents linear regressions generated from training data during cross-validation.

Over the continent, inter-model variability in the lapse-rate feedback could explain variability in warming between downscaled models. For example, despite its high ECS, MAR-UKESM has weak warming over the plateau driven by low ΔD_θ (Table S5). We attribute this to a weak lapse-rate feedback considering the low slope in MAR-UKESM's linear regression of ΔD_θ versus N^2 (Fig. 9a, Table S8). Likewise, weak lapse-rate feedbacks over the ice shelves in MAR-IPSL and MAR-MPI would explain their low ΔD_θ values over the ice shelves (Table S5) given the low ΔD_θ–N^2 slopes in these simulations' ice shelves (Fig. 9c, Table S8). These low ΔD_θ values occur despite the high ECS in UKESM and IPSL, so ECS also appears to be a somewhat poor predictor of continental near-surface warming for these four models. These results in ΔD_θ are not necessarily shared by the polar amplification results. For instance, although the plateau in MAR-UKESM does in fact report particularly low PAF driven by its low ΔD_θ and high ECS, the PAF over the ice shelves is fairly similar across the models. The strong normalizing effect of global warming in the PAF calculation dilutes the effects of ΔD_θ on PAF. To summarize, variability

https://doi.org/10.5194/egusphere-2026-4032
Preprint. Discussion started: 28 August 2026

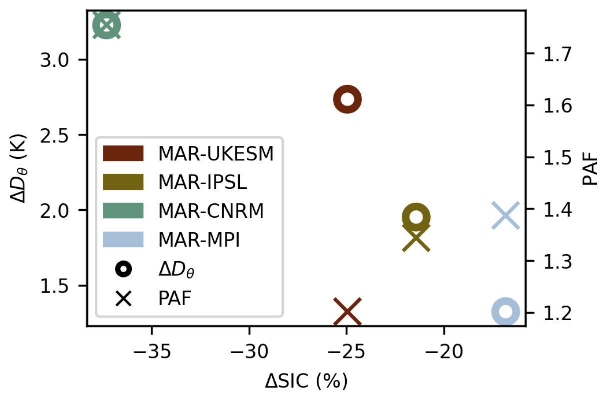

Figure 10. Mean 21st-century change in July potential temperature deficit (ΔD_θ) and polar amplification factor (PAF) versus July sea ice loss (ΔSIC) throughout the whole study area.

in the strength of the lapse-rate feedback between downscaled GCM simulations may contribute to inter-model variability in ΔD_θ.

4 Discussion

Our study reveals that surface processes are important in driving spatial variability in Antarctic near-surface warming and, in turn, amplification. This is particularly true over the ocean surrounding Antarctica. Here, the change in the surface temperature inversion is responsible for nearly half of the total warming in the Antarctic sea ice region (Table 3). Meanwhile, over the continent, our results indicate that the lapse-rate feedback contributes substantially to Antarctic warming given that greater ΔD_θ is associated with higher present-day static stability (Sect. 3.4), which aligns with previous research (e.g., Graversen et al., 2014; Cai et al., 2021; Liu et al., 2022). However, sea ice loss contributes more strongly to Antarctic amplification than the net effect of continental surface mechanisms (including the continental lapse-rate feedback) given the particularly high Antarctic amplification reported over the sea ice (Table 3).

Explaining why the Arctic is expected to experience greater polar amplification than the Antarctic is an ongoing challenge (e.g., Cai et al., 2021). For example, under transient CO_2 doubling, Taylor et al. (2013) project that the surface of the northern polar region will warm 2.3 times more than the global average on an annual timescale while the southern polar region will warm 1.6 times more. Stuecker et al. (2018) simulate Arctic warming under abrupt CO_2 quadrupling that is 2.50 times greater than tropical warming at an annual scale as opposed to Antarctic warming that is 1.70 times greater. During winter under SSP5-8.5, Xie et al. (2022) report that the Arctic warms 1.38 times faster than the global mean while the Antarctic warms 1.18 times as fast. We report a multi-model mean PAF of 1.6 over the continent and sea ice, although we stress that the amplification values from the literature are calculated using various methods. Since the Arctic is mainly ocean, it may experience greater amplification because of its greater relative area for sea ice loss given the strong contribution of sea ice loss to amplification. It

https://doi.org/10.5194/egusphere-2026-4032
Preprint. Discussion started: 28 August 2026

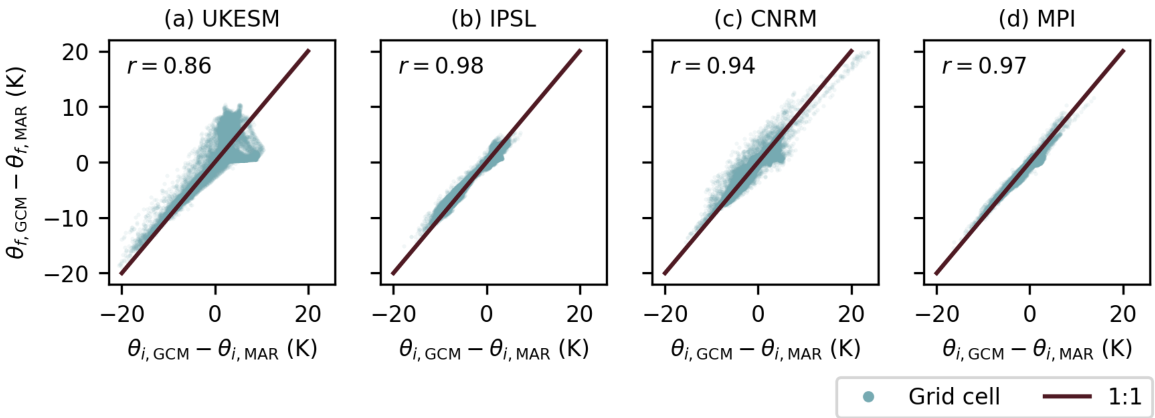

Figure 11. Biases in potential temperature between downscaled and non-downscaled GCM simulations. $\theta_{i,\mathrm{MAR}}$ and $\theta_{f,\mathrm{MAR}}$ respectively represent mean present-day and future July potential temperature (θ) in the downscaled GCM simulations. $\theta_{i,\mathrm{GCM}}$ and $\theta_{f,\mathrm{GCM}}$ represent the same quantities prior to downscaling from CMIP6 data. The plots represent the entire study area. r indicates Pearson's correlation coefficient.

would be valuable to repeat our analysis over the Arctic to quantify its amplification in comparison and identify drivers behind its warming.

We also emphasize the value of downscaling when simulating the Antarctic boundary layer. Figure 2b shows that there are substantial biases in the non-downscaled potential temperature relative to the MAR simulations. If biases in temperature between downscaled and non-downscaled GCMs remained constant over time, then both downscaled and non-downscaled GCM simulations would produce the same warming estimates. However, Fig. 11 shows that these biases do not remain constant from the present-day to future time period across the four GCMs we use. If they did, the figure would show all points lying along a 1:1 line with $r = 1$ between present and future biases, where r is Pearson's correlation coefficient. Instead, we observe some scatter, indicating that the biases differ from present to future. We note that r between the present and future biases only drops as low as $r = 0.86$, so the biases often remain quite similar. Nonetheless, the bias can sometimes differ by about 5 K or more (e.g., Fig. 11a) between the present and future periods despite these high r values. This reflects the importance of downscaling GCMs with RCMs when simulating Antarctic warming and amplification given that RCMs are well suited to Antarctic boundary layer conditions (e.g., Davrinche et al., 2025; Gilbert et al., 2026).

One limitation of our study is that MAR has no atmosphere–ocean coupling. Therefore, in our simulations, oceanic processes like sea ice do not evolve in response to changes in the atmosphere simulated by MAR. Rather, they evolve in response to the atmosphere in the GCM itself prior to downscaling since the GCMs are coupled. Similarly, we discuss relationships between each non-downscaled GCM's ECS and its corresponding downscaled simulation's near-surface warming. However, the effective ECS of MAR in each simulation may differ from the ECS of the driving GCM because some feedbacks are represented differently in MAR (e.g., cloud feedbacks). Although we cannot calculate the ECS values of the MAR simulations given that they only simulate the Antarctic, the mean reported near-surface warming throughout the entire study area is 0.1 K

https://doi.org/10.5194/egusphere-2026-4032
Preprint. Discussion started: 28 August 2026

higher in each of MAR-UKESM, MAR-CNRM, and MAR-MPI compared to their corresponding non-downscaled GCMs. Meanwhile, MAR-IPSL reports lower warming than its non-downscaled version by 0.2 K. We must take these limitations into account when interpreting MAR outputs.

Furthermore, this study has implications for paleoclimate research. We expect both cloud-based and surface- or subsurface-based temperature proxies (i.e., proxies that depend on the condensation temperature versus those that depend on the surface temperature) to capture the surface background warming signal ($\Delta\theta_0$). This is because the change in the background potential temperature would presumably remain similar throughout the atmospheric profile. Meanwhile, the vertical separation between these two types of proxies could lead to a discrepancy in their temperature records, as cloud-based proxies would not capture changes in the surface inversion strength (ΔD_θ), while surface- or subsurface-based proxies would capture these changes (Servettaz et al., 2023). If ΔD_θ always changed in a constant ratio with $\Delta\theta_0$, then this vertical discrepancy would not be a problem, as cloud-based proxy temperature records could be converted to match surface- or subsurface-based proxy temperature records based on that ratio. However, the contribution of the surface temperature inversion to warming is not spatially uniform (Fig. 7d), which implies that $\Delta\theta_0$ and ΔD_θ do not follow a constant ratio in space (Buizert et al., 2021). For instance, the inversion strength contributes 29 % of warming at the EPICA Dome C ice core site in the plateau interior, a region in which ΔD_θ is fairly high. In contrast, the WAIS Divide site is less sensitive to change in the inversion strength (10 %) and more representative of the background warming signal, which is likely because it is situated in a region of low ΔD_θ in West Antarctica (Fig. 7c). Table S10 shows how the inversion contribution varies widely between these ice core sites and four others.

5 Conclusions

This study demonstrates the role of the surface temperature inversion in 21st-century Antarctic near-surface warming during the month of July by dynamically downscaling four CMIP6 GCMs using an RCM to simulate the atmospheric boundary layer. In total, 28 % of the near-surface warming from 1980–2000 to 2080–2100 is caused by the change in the surface inversion strength, which accounts for 16 % of warming over the continent and 41 % of warming over the sea ice. The mean Antarctic warming signal is mainly driven by background warming due to large-scale processes, while spatial variability in this warming is largely explained by the weakening of the surface temperature inversion. Temporal changes in SIC can successfully predict the inversion strength during July in 2080–2100, so we conclude that SIC is an important control on warming and amplification in the Southern Ocean. Furthermore, there is a positive relationship between the 21st-century change in the inversion strength and the present-day static stability over the continent. Linear regressions can predict the change in the inversion strength from present-day N^2 over the plateau and the Ronne and Ross Ice Shelves with some success. These results align with the polar lapse-rate feedback. Our findings provide insight into how sea ice loss and the lapse-rate feedback play an important role in shaping Antarctic warming and amplification.

These results have important implications for our understanding of past and future climate changes in Antarctica. In particular, sea ice loss is a major driver of the region's warming. Differing sea ice loss patterns explain the variability in total warming between downscaled GCMs. Sea ice could explain why Arctic amplification is projected to be greater than Antarctic

https://doi.org/10.5194/egusphere-2026-4032
Preprint. Discussion started: 28 August 2026

amplification: The Arctic has a greater relative capacity for sea ice loss given that it is mainly oceanic. The surface temperature inversion could also explain discrepancies between temperature records reconstructed using ice cores, as certain proxies depend on surface conditions while others do not, and certain locations are more sensitive to temporal changes in the surface temperature inversion. To conclude, understanding how surface temperature inversions amplify Antarctic warming helps reveal how and why polar regions are warming faster than the rest of the world.

Code and data availability. Code and data to reproduce the figures and tables of this article are to be made publicly available after peer review.

Appendix A: Calculation of the potential temperature deficit

We separate θ into the background potential temperature (θ_0) and the potential temperature deficit (D_θ), where $\theta = \theta_0 + D_\theta$ (Fig. A1). θ_0 is calculated by linearizing the potential temperature profile in the upper atmosphere from a certain height H_{min} up to 350 hPa. H_{min} represents the height below which the following threshold is reached:

$$|\frac{\partial \theta}{\partial z} - \gamma_{350-500}| > 4\gamma_{350-500} \tag{A1}$$

where $\gamma_{350-500}$ represents the slope of potential temperature linearized between 500 hPa and 350 hPa. Then, throughout the atmospheric profile, θ_0 is calculated as:

$$\theta_0(x,y,z) = \gamma_0(x,y) \cdot z + \tau_0(x,y) \tag{A2}$$

where γ_0 represents the slope of the linearization from H_{min} to 350 hPa and τ_0 represents the θ_0 intercept at the surface from the linearization. We assume that θ_0 is independent of surface processes and instead controlled solely by large-scale pressure gradients (van den Broeke and van Lipzig, 2003; Davrinche et al., 2024). D_θ is then calculated by subtracting θ_0 from θ. Please see Davrinche et al. (2024) for the full temperature decomposition procedure.

Author contributions. AO conceptualized the project. CA configured the MAR model, and CD and CA conducted model simulations. BT post-processed all data, wrote the code to conduct the analysis, and created all figures and tables. CD curated the data and supported the coding process. BT wrote the study's initial draft with AO's feedback, while subsequent drafts were edited by all authors.

Competing interests. The authors declare that they have no conflict of interest.

Acknowledgements. We acknowledge funding from the Natural Sciences and Engineering Research Council of Canada (NSERC) and The University of British Columbia, which supported Ben Tyler with an Undergraduate Student Research Award in 2025. The Agence Nationale

https://doi.org/10.5194/egusphere-2026-4032
Preprint. Discussion started: 28 August 2026

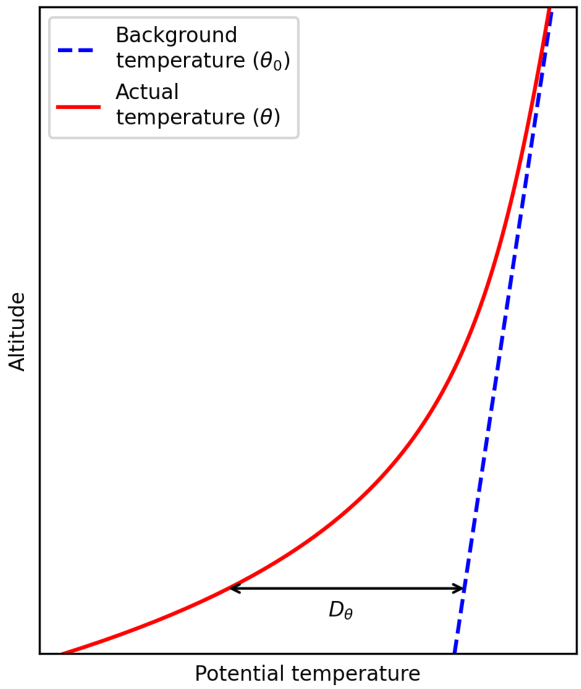

Figure A1. Typical profile of potential temperature (θ), background potential temperature (θ_0), and potential temperature deficit (D_θ) in the study area. This illustration is based on Fig. 11 in Bintanja et al. (2014) and Fig. 2 in Davrinche et al. (2024). For example, on the Adélie Land transect in Fig. 5, -15 K is a typical near-surface D_θ value, and 1 km is a typical altitude above the surface at which θ and θ_0 converge (Davrinche et al., 2024).

de la Recherche JCJC Katabatic project (grant no. ANR19-CE01-0020-01 for Anaïs Orsi) and NSERC Discovery (grant no. DGERC-2021-00213) also funded the project. We also acknowledge Cécile Agosta (Laboratoire des Sciences du Climat et de l'Environnement) and Christoph Kittel (Université de Liège, postdoctoral fellow of the Fonds de la Recherche Scientifique de Belgique F.R.S.–FNRS) for configuring MAR, conducting simulations, and providing advice during writing. To process the MAR data, this study benefited from the IPSL Mesocentre ESPRI facility which is supported by CNRS, UPMC, Labex L-IPSL, CNES and École Polytechnique. Computational resources were also provided by the Consortium des Équipements de Calcul Intensif (CÉCI), funded by the Fonds de la Recherche Scientifique de Belgique (F.R.S.–FNRS) under Grant No. 2.5020.11, and Lucia, the Tier-1 supercomputer of the Walloon Region, infrastructure funded by the Walloon Region under the grant agreement n°1910247. We acknowledge Xavier Fettweis' role in MAR's development and maintenance (Université de Liège). We are grateful for the World Climate Research Programme and its associated modelling groups for generating and sharing CMIP6 data, the Earth System Grid Federation (ESGF) for facilitating CMIP6 data access, and the organizations that fund CMIP6 and ESGF. Ben Tyler used generative artificial intelligence (ChatGPT, Google Gemini, Google Search AI) to help write code and operate software, help design visualizations, assist in navigating literature, and help prevent errors in the data analysis. We thank Crameri et al. (2020) for colour schemes that we use in our figures.

References

Agosta, C., Amory, C., Kittel, C., Orsi, A., Favier, V., Gallée, H., van den Broeke, M. R., Lenaerts, J. T. M., van Wessem, J. M., van de Berg, W. J., and Fettweis, X.: Estimation of the Antarctic surface mass balance using the regional climate model MAR (1979–2015) and identification of dominant processes, Cryosphere, 13, 281–296, https://doi.org/10.5194/tc-13-281-2019, 2019.

Alexeev, V. A., Langen, P. L., and Bates, J. R.: Polar amplification of surface warming on an aquaplanet in "ghost forcing" experiments without sea ice feedbacks, Clim. Dyn., 24, 655–666, https://doi.org/10.1007/s00382-005-0018-3, 2005.

Amory, C., Kittel, C., Le Toumelin, L., Agosta, C., Delhasse, A., Favier, V., and Fettweis, X.: Performance of MAR (v3.11) in simulating the drifting-snow climate and surface mass balance of Adélie Land, East Antarctica, Geosci. Model Dev., 14, 3487–3510, https://doi.org/10.5194/gmd-14-3487-2021, 2021.

Andreas, E. L., Claffy, K. J., and Makshtas, A. P.: Low-level atmospheric jets and inversions over the western Weddell Sea, Bound.-Layer Meteorol., 97, 459–486, https://doi.org/10.1023/A:1002793831076, 2000.

Baas, P., van de Wiel, B. J. H., van Meijgaard, E., Vignon, E., Genthon, C., van der Linden, S. J. A., and de Roode, S. R.: Transitions in the wintertime near-surface temperature inversion at Dome C, Antarctica, Q. J. R. Meteorol. Soc., 145, 930–946, https://doi.org/10.1002/qj.3450, 2019.

Bender, M. L., Floch, G., Chappellaz, J., Suwa, M., Barnola, J.-M., Blunier, T., Dreyfus, G., Jouzel, J., and Parrenin, F.: Gas age–ice age differences and the chronology of the Vostok ice core, 0–100 ka, J. Geophys. Res.: Atmos., 111, D21115, https://doi.org/10.1029/2005JD006488, 2006.

Bintanja, R., Graversen, R. G., and Hazeleger, W.: Arctic winter warming amplified by the thermal inversion and consequent low infrared cooling to space, Nat. Geosci., 4, 758–761, https://doi.org/10.1038/ngeo1285, 2011.

Bintanja, R., van der Linden, E. C., and Hazeleger, W.: Boundary layer stability and Arctic climate change: A feedback study using EC-Earth, Clim. Dyn., 39, 2659–2673, https://doi.org/10.1007/s00382-011-1272-1, 2012.

Bintanja, R., Severijns, C., Haarsma, R., and Hazeleger, W.: The future of Antarctica's surface winds simulated by a high-resolution global climate model: 2. Drivers of 21st century changes, J. Geophys. Res.: Atmos., 119, 7160–7178, https://doi.org/10.1002/2013JD020848, 2014.

Boeke, R. C., Taylor, P. C., and Sejas, S. A.: On the nature of the Arctic's positive lapse-rate feedback, Geophys. Res. Lett., 48, e2020GL091109, https://doi.org/10.1029/2020GL091109, 2021.

Boucher, O., Servonnat, J., Albright, A. L., Aumont, O., Balkanski, Y., Bastrikov, V., Bekki, S., Bonnet, R., Bony, S., Bopp, L., Braconnot, P., Brockmann, P., Cadule, P., Caubel, A., Cheruy, F., Codron, F., Cozic, A., Cugnet, D., D'Andrea, F., Davini, P., de Lavergne, C., Denvil, S., Deshayes, J., Devilliers, M., Ducharne, A., Dufresne, J.-L., Dupont, E., Éthé, C., Fairhead, L., Falletti, L., Flavoni, S., Foujols, M.-A., Gardoll, S., Gastineau, G., Ghattas, J., Grandpeix, J.-Y., Guenet, B., Guez, Lionel, E., Guilyardi, E., Guimberteau, M., Hauglustaine, D., Hourdin, F., Idelkadi, A., Joussaume, S., Kageyama, M., Khodri, M., Krinner, G., Lebas, N., Levavasseur, G., Lévy, C., Li, L., Lott, F., Lurton, T., Luyssaert, S., Madec, G., Madeleine, J.-B., Maignan, F., Marchand, M., Marti, O., Mellul, L., Meurdesoif, Y., Mignot, J., Musat, I., Ottlé, C., Peylin, P., Planton, Y., Polcher, J., Rio, C., Rochetin, N., Rousset, C., Sepulchre, P., Sima, A., Swingedouw, D., Thiéblemont, R., Traore, A. K., Vancoppenolle, M., Vial, J., Vialard, J., Viovy, N., and Vuichard, N.: Presentation and evaluation of the IPSL-CM6A-LR climate model, J. Adv. Model. Earth Syst., 12, e2019MS002010, https://doi.org/10.1029/2019MS002010, 2020.

Bracegirdle, T. J., Krinner, G., Tonelli, M., Haumann, F. A., Naughten, K. A., Rackow, T., Roach, L. A., and Wainer, I.: Twenty first century changes in Antarctic and Southern Ocean surface climate in CMIP6, Atmos. Sci. Lett., 21, e984, https://doi.org/10.1002/asl.984, 2020.

https://doi.org/10.5194/egusphere-2026-4032
Preprint. Discussion started: 28 August 2026

Budyko, M. I.: The effect of solar radiation variations on the climate of the Earth, Tellus, 21, 611–619, https://doi.org/10.1111/j.2153-3490.1969.tb00466.x, 1969.

Buizert, C., Fudge, T. J., Roberts, W. H. G., Steig, E. J., Sherriff-Tadano, S., Ritz, C., Lefebvre, E., Edwards, J., Kawamura, K., Oyabu, I., Motoyama, H., Kahle, E. C., Jones, T. R., Abe-Ouchi, A., Obase, T., Martin, C., Corr, H., Severinghaus, J. P., Beaudette, R., Epifanio, J. A., Brook, E. J., Martin, K., Chappellaz, J., Aoki, S., Nakazawa, T., Sowers, T. A., Alley, R. B., Ahn, J., Sigl, M., Severi, M., Dunbar, N. W., Svensson, A., Fegyveresi, J. M., He, C., Liu, Z., Zhu, J., Otto-Bliesner, B. L., Lipenkov, V. Y., Kageyama, M., and Schwander, J.: Antarctic surface temperature and elevation during the Last Glacial Maximum, Science, 372, 1097–1101, https://doi.org/10.1126/science.abd2897, 2021.

Cai, M. and Lu, J.: Dynamical greenhouse-plus feedback and polar warming amplification. Part II: Meridional and vertical asymmetries of the global warming, Clim. Dyn., 29, 375–391, https://doi.org/10.1007/s00382-007-0238-9, 2007.

Cai, S., Hsu, P.-C., and Liu, F.: Changes in polar amplification in response to increasing warming in CMIP6, Atmos. Ocean. Sci. Lett., 14, 100043, https://doi.org/10.1016/j.aosl.2021.100043, 2021.

Clifford, P., Richardson, S., and Hemon, D.: Assessing the significance of the correlation between two spatial processes, Biometrics, 45, 123–134, https://doi.org/10.2307/2532039, 1989.

Connolley, W. M.: The Antarctic temperature inversion, Int. J. Climatol., 16, 1333–1342, https://doi.org/10.1002/(SICI)1097-0088(199612)16:12<1333::AID-JOC96>3.0.CO;2-6, 1996.

Crameri, F., Shephard, G. E., and Heron, P. J.: The misuse of colour in science communication, Nat. Commun., 11, 5444, https://doi.org/10.1038/s41467-020-19160-7, 2020.

Dai, A., Luo, D., Song, M., and Liu, J.: Arctic amplification is caused by sea-ice loss under increasing CO_2, Nat. Commun., 10, 121, https://doi.org/10.1038/s41467-018-07954-9, 2019.

Dale, M. R. T. and Fortin, M.-J.: Spatial Analysis: A Guide for Ecologists, Cambridge University Press, 2 edn., https://doi.org/10.1017/CBO9780511978913, 2014.

Davrinche, C., Orsi, A., Agosta, C., Amory, C., and Kittel, C.: Understanding the drivers of near-surface winds in Adélie Land, East Antarctica, Cryosphere, 18, 2239–2256, https://doi.org/10.5194/tc-18-2239-2024, 2024.

Davrinche, C., Orsi, A., Amory, C., Kittel, C., and Agosta, C.: Future changes in Antarctic near-surface winds: Regional variability and key drivers under a high-emission scenario, Cryosphere, 19, 6023–6042, https://doi.org/10.5194/tc-19-6023-2025, 2025.

Dutilleul, P., Clifford, P., Richardson, S., and Hemon, D.: Modifying the t test for assessing the correlation between two spatial processes, Biometrics, 49, 305–314, https://doi.org/10.2307/2532625, 1993.

Eyring, V., Bony, S., Meehl, G. A., Senior, C. A., Stevens, B., Stouffer, R. J., and Taylor, K. E.: Overview of the Coupled Model Intercomparison Project Phase 6 (CMIP6) experimental design and organization, Geosci. Model Dev., 9, 1937–1958, https://doi.org/10.5194/gmd-9-1937-2016, 2016.

Feldl, N. and Roe, G. H.: The nonlinear and nonlocal nature of climate feedbacks, J. Clim., 26, 8289–8304, https://doi.org/10.1175/JCLI-D-12-00631.1, 2013.

Feldl, N., Po-Chedley, S., Singh, H. K. A., Hay, S., and Kushner, P. J.: Sea ice and atmospheric circulation shape the high-latitude lapse rate feedback, npj Climate and Atmospheric Science, 3, 41, https://doi.org/10.1038/s41612-020-00146-7, 2020.

Flannery, B. P.: Energy balance models incorporating transport of thermal and latent energy, J. Atmos. Sci., 41, 414–421, https://doi.org/10.1175/1520-0469(1984)041<0414:EBMITO>2.0.CO;2, 1984.

https://doi.org/10.5194/egusphere-2026-4032
Preprint. Discussion started: 28 August 2026

Flynn, C. M. and Mauritsen, T.: On the climate sensitivity and historical warming evolution in recent coupled model ensembles, Atmos. Chem. Phys., 20, 7829–7842, https://doi.org/10.5194/acp-20-7829-2020, 2020.

Fretwell, P., Pritchard, H. D., Vaughan, D. G., Bamber, J. L., Barrand, N. E., Bell, R., Bianchi, C., Bingham, R. G., Blankenship, D. D., Casassa, G., Catania, G., Callens, D., Conway, H., Cook, A. J., Corr, H. F. J., Damaske, D., Damm, V., Ferraccioli, F., Forsberg, R., Fujita, S., Gim, Y., Gogineni, P., Griggs, J. A., Hindmarsh, R. C. A., Holmlund, P., Holt, J. W., Jacobel, R. W., Jenkins, A., Jokat, W., Jordan, T., King, E. C., Kohler, J., Krabill, W., Riger-Kusk, M., Langley, K. A., Leitchenkov, G., Leuschen, C., Luyendyk, B. P., Matsuoka, K., Mouginot, J., Nitsche, F. O., Nogi, Y., Nost, O. A., Popov, S. V., Rignot, E., Rippin, D. M., Rivera, A., Roberts, J., Ross, N., Siegert, M. J., Smith, A. M., Steinhage, D., Studinger, M., Sun, B., Tinto, B. K., Welch, B. C., Wilson, D., Young, D. A., Xiangbin, C., and Zirizzotti, A.: Bedmap2: Improved ice bed, surface and thickness datasets for Antarctica, Cryosphere, 7, 375–393, https://doi.org/10.5194/tc-7-375-2013, 2013.

Gallée, H.: Simulation of the mesocyclonic activity in the Ross Sea, Antarctica, Mon. Weather Rev., 123, 2051–2069, https://doi.org/10.1175/1520-0493(1995)123<2051:SOTMAI>2.0.CO;2, 1995.

Gallée, H. and Schayes, G.: Development of a three-dimensional meso-γ primitive equation model: Katabatic winds simulation in the area of Terra Nova Bay, Antarctica, Mon. Weather Rev., 122, 671–685, https://doi.org/10.1175/1520-0493(1994)122<0671:DOATDM>2.0.CO;2, 1994.

Gilbert, E., Torres-Alavez, J. A., Hofsteenge, M. G., van de Berg, W. J., Boberg, F., Christensen, O. B., van Dalum, C. T., Fettweis, X., Gumber, S., Hansen, N., Kittel, C., Lambin, C., Maure, D., Mottram, R., Olesen, M., Orr, A., Phillips, T., van Tiggelen, M., Verro, K., and Mooney, P. A.: The PolarRES dataset: A state-of-the-art regional climate model ensemble for understanding Antarctic climate, Cryosphere, 20, 2629–2658, https://doi.org/10.5194/tc-20-2629-2026, 2026.

Goosse, H., Kay, J. E., Armour, K. C., Bodas-Salcedo, A., Chepfer, H., Docquier, D., Jonko, A., Kushner, P. J., Lecomte, O., Massonnet, F., Park, H.-S., Pithan, F., Svensson, G., and Vancoppenolle, M.: Quantifying climate feedbacks in polar regions, Nat. Commun., 9, 1919, https://doi.org/10.1038/s41467-018-04173-0, 2018.

Graversen, R. G. and Langen, P. L.: On the role of the atmospheric energy transport in $2 \times CO_2$–induced polar amplification in CESM1, J. Clim., 32, 3941–3956, https://doi.org/10.1175/JCLI-D-18-0546.1, 2019.

Graversen, R. G., Langen, P. L., and Mauritsen, T.: Polar amplification in CCSM4: Contributions from the lapse rate and surface albedo feedbacks, J. Clim., 27, 4433–4450, https://doi.org/10.1175/JCLI-D-13-00551.1, 2014.

Hahn, L. C., Armour, K. C., Zelinka, M. D., Bitz, C. M., and Donohoe, A.: Contributions to polar amplification in CMIP5 and CMIP6 models, Front. Earth Sci., 9, 710036, https://doi.org/10.3389/feart.2021.710036, 2021.

Haining, R.: Bivariate correlation with spatial data, Geogr. Anal., 23, 210–227, https://doi.org/10.1111/j.1538-4632.1991.tb00235.x, 1991.

Hall, A.: The role of surface albedo feedback in climate, J. Clim., 17, 1550–1568, https://doi.org/10.1175/1520-0442(2004)017<1550:TROSAF>2.0.CO;2, 2004.

Helsen, M. M., van de Wal, R. S. W., van den Broeke, M. R., van As, D., Meijer, H. A. J., and Reijmer, C. H.: Oxygen isotope variability in snow from western Dronning Maud Land, Antarctica and its relation to temperature, Tellus B, 57, 423–435, https://doi.org/10.1111/j.1600-0889.2005.00162.x, 2005.

Henry, M. and Merlis, T. M.: The role of the nonlinearity of the Stefan–Boltzmann Law on the structure of radiatively forced temperature change, J. Clim., 32, 335–348, https://doi.org/10.1175/JCLI-D-17-0603.1, 2019.

Holland, M. M. and Bitz, C. M.: Polar amplification of climate change in coupled models, Clim. Dyn., 21, 221–232, https://doi.org/10.1007/s00382-003-0332-6, 2003.

https://doi.org/10.5194/egusphere-2026-4032
Preprint. Discussion started: 28 August 2026

Holtslag, A. A. M.: Boundary layer (atmospheric) and air pollution | Modeling and parameterization, in: Encyclopedia of Atmospheric Sciences, edited by: North, G. R., Pyle, J., and Zhang, F., Academic Press, 2 edn., 265–273, https://doi.org/10.1016/B978-0-12-382225-3.00087-6, 2015.

Hudson, S. R. and Brandt, R. E.: A look at the surface-based temperature inversion on the Antarctic Plateau, J. Clim., 18, 1673–1696, https://doi.org/10.1175/JCLI3360.1, 2005.

Hwang, Y.-T., Frierson, D. M. W., and Kay, J. E.: Coupling between Arctic feedbacks and changes in poleward energy transport, Geophys. Res. Lett., 38, L17704, https://doi.org/10.1029/2011GL048546, 2011.

IPCC: Climate Change 2021 – The Physical Science Basis: Working Group I Contribution to the Sixth Assessment Report of the Intergovernmental Panel on Climate Change, Cambridge University Press, 1 edn., https://doi.org/10.1017/9781009157896, 2023.

Jouzel, J. and Merlivat, L.: Deuterium and oxygen 18 in precipitation: Modeling of the isotopic effects during snow formation, J. Geophys. Res.: Atmos., 89, 11 749–11 757, https://doi.org/10.1029/JD089iD07p11749, 1984.

Kittel, C., Amory, C., Agosta, C., Jourdain, N. C., Hofer, S., Delhasse, A., Doutreloup, S., Huot, P.-V., Lang, C., Fichefet, T., and Fettweis, X.: Diverging future surface mass balance between the Antarctic ice shelves and grounded ice sheet, Cryosphere, 15, 1215–1236, https://doi.org/10.5194/tc-15-1215-2021, 2021.

Kruskal, W. H. and Wallis, W. A.: Use of ranks in one-criterion variance analysis, Journal of the American Statistical Association, 47, 583–621, https://doi.org/10.2307/2280779, 1952.

Langen, P. L., Graversen, R. G., and Mauritsen, T.: Separation of contributions from radiative feedbacks to polar amplification on an aquaplanet, J. Clim., 25, 3010–3024, https://doi.org/10.1175/JCLI-D-11-00246.1, 2012.

Legendre, P. and Legendre, L.: Numerical Ecology, vol. 24 of *Developments in Environmental Modelling*, Elsevier, 3 edn., ISBN 978-0-444-53868-0, 2012.

Linke, O., Quaas, J., Baumer, F., Becker, S., Chylik, J., Dahlke, S., Ehrlich, A., Handorf, D., Jacobi, C., Kalesse-Los, H., Lelli, L., Mehrdad, S., Neggers, R. A. J., Riebold, J., Saavedra Garfias, P., Schnierstein, N., Shupe, M. D., Smith, C., Spreen, G., Verneuil, B., Vinjamuri, K. S., Vountas, M., and Wendisch, M.: Constraints on simulated past Arctic amplification and lapse rate feedback from observations, Atmos. Chem. Phys., 23, 9963–9992, https://doi.org/10.5194/acp-23-9963-2023, 2023.

Liu, J., Luo, Y., and Liu, F.: Externally forced symmetric warming in the Arctic and Antarctic during the second half of the twentieth century, Geosci. Lett., 9, 16, https://doi.org/10.1186/s40562-022-00226-x, 2022.

Lu, J. and Cai, M.: Quantifying contributions to polar warming amplification in an idealized coupled general circulation model, Clim. Dyn., 34, 669–687, https://doi.org/10.1007/s00382-009-0673-x, 2010.

Manabe, S. and Stouffer, R. J.: Sensitivity of a global climate model to an increase of CO_2 concentration in the atmosphere, J. Geophys. Res.: Oceans, 85, 5529–5554, https://doi.org/10.1029/JC085iC10p05529, 1980.

Manabe, S. and Wetherald, R. T.: The effects of doubling the CO_2 concentration on the climate of a general circulation model, J. Atmos. Sci., 32, 3–15, https://doi.org/10.1175/1520-0469(1975)032<0003:TEODTC>2.0.CO;2, 1975.

Mauritsen, T., Bader, J., Becker, T., Behrens, J., Bittner, M., Brokopf, R., Brovkin, V., Claussen, M., Crueger, T., Esch, M., Fast, I., Fiedler, S., Fläschner, D., Gayler, V., Giorgetta, M., Goll, D. S., Haak, H., Hagemann, S., Hedemann, C., Hohenegger, C., Ilyina, T., Jahns, T., Jimenéz-de-la-Cuesta, D., Jungclaus, J., Kleinen, T., Kloster, S., Kracher, D., Kinne, S., Kleberg, D., Lasslop, G., Kornblueh, L., Marotzke, J., Matei, D., Meraner, K., Mikolajewicz, U., Modali, K., Möbis, B., Müller, W. A., Nabel, J. E. M. S., Nam, C. C. W., Notz, D., Nyawira, S.-S., Paulsen, H., Peters, K., Pincus, R., Pohlmann, H., Pongratz, J., Popp, M., Raddatz, T. J., Rast, S., Redler, R., Reick, C. H., Rohrschneider, T., Schemann, V., Schmidt, H., Schnur, R., Schulzweida, U., Six, K. D., Stein, L., Stemmler, I., Stevens,

https://doi.org/10.5194/egusphere-2026-4032
Preprint. Discussion started: 28 August 2026

B., von Storch, J.-S., Tian, F., Voigt, A., Vrese, P., Wieners, K.-H., Wilkenskjeld, S., Winkler, A., and Roeckner, E.: Developments in the MPI-M Earth System Model version 1.2 (MPI-ESM1.2) and its response to increasing CO_2, J. Adv. Model. Earth Syst., 11, 998–1038, https://doi.org/10.1029/2018MS001400, 2019.

O'Neill, B. C., Tebaldi, C., van Vuuren, D. P., Eyring, V., Friedlingstein, P., Hurtt, G., Knutti, R., Kriegler, E., Lamarque, J.-F., Lowe, J., Meehl, G. A., Moss, R., Riahi, K., and Sanderson, B. M.: The Scenario Model Intercomparison Project (ScenarioMIP) for CMIP6, Geosci. Model Dev., 9, 3461–3482, https://doi.org/10.5194/gmd-9-3461-2016, 2016.

Parish, T. R. and Bromwich, D. H.: A case study of Antarctic katabatic wind interaction with large-scale forcing*, Mon. Weather Rev., 126, 199–209, https://doi.org/10.1175/1520-0493(1998)126<0199:ACSOAK>2.0.CO;2, 1998.

Pavelsky, T. M., Boé, J., Hall, A., and Fetzer, E. J.: Atmospheric inversion strength over polar oceans in winter regulated by sea ice, Clim. Dyn., 36, 945–955, https://doi.org/10.1007/s00382-010-0756-8, 2011.

Pedregosa, F., Varoquaux, G., Gramfort, A., Michel, V., Thirion, B., Grisel, O., Blondel, M., Prettenhofer, P., Weiss, R., Dubourg, V., Vanderplas, J., Passos, A., Cournapeau, D., Brucher, M., Perrot, M., and Duchesnay, É.: Scikit-learn: Machine learning in Python, J. Mach. Learn. Res., 12, 2825–2830, 2011.

Phillpot, H. R. and Zillman, J. W.: The surface temperature inversion over the Antarctic Continent, J. Geophys. Res., 75, 4161–4169, https://doi.org/10.1029/JC075i021p04161, 1970.

Pietroni, I., Argentini, S., and Petenko, I.: One year of surface-based temperature inversions at Dome C, Antarctica, Bound.-Layer Meteorol., 150, 131–151, https://doi.org/10.1007/s10546-013-9861-7, 2014.

Pithan, F. and Mauritsen, T.: Arctic amplification dominated by temperature feedbacks in contemporary climate models, Nat. Geosci., 7, 181–184, https://doi.org/10.1038/ngeo2071, 2014.

Previdi, M., Janoski, T. P., Chiodo, G., Smith, K. L., and Polvani, L. M.: Arctic amplification: A rapid response to radiative forcing, Geophys. Res. Lett., 47, e2020GL089933, https://doi.org/10.1029/2020GL089933, 2020.

Rinke, A., Dethloff, K., Dorn, W., Handorf, D., and Moore, J. C.: Simulated Arctic atmospheric feedbacks associated with late summer sea ice anomalies, J. Geophys. Res.: Atmos., 118, 7698–7714, https://doi.org/10.1002/jgrd.50584, 2013.

Riordan, A. J.: Variations of temperature and air motion in the 0- to 32-meter layer at Plateau Station, Antarctica, in: Meteorological Studies at Plateau Station, Antarctica, edited by: Dalrymple, P. C., Riordan, A. J., Riordan, A., Riordan, A. J., Weller, G., Lettau, H. H., Lettau, H., Stroschein, L. A., Kundla, L. S., Stroschein, L. A., Kuhn, M., Schwerdtfeger, P., Lile, R. C., and Radok, U., American Geophysical Union, 113–127, https://doi.org/10.1029/AR025, 1977.

Roberts, D. R., Bahn, V., Ciuti, S., Boyce, M. S., Elith, J., Guillera-Arroita, G., Hauenstein, S., Lahoz-Monfort, J. J., Schröder, B., Thuiller, W., Warton, D. I., Wintle, B. A., Hartig, F., and Dormann, C. F.: Cross-validation strategies for data with temporal, spatial, hierarchical, or phylogenetic structure, Ecography, 40, 913–929, https://doi.org/10.1111/ecog.02881, 2017.

Ruman, C. J., Monahan, A. H., and Sushama, L.: Climatology of Arctic temperature inversions in current and future climates, Theor. Appl. Climatol., 150, 121–134, https://doi.org/10.1007/s00704-022-04147-9, 2022.

Salzmann, M.: The polar amplification asymmetry: Role of Antarctic surface height, Earth Syst. Dyn., 8, 323–336, https://doi.org/10.5194/esd-8-323-2017, 2017.

Screen, J. A. and Simmonds, I.: The central role of diminishing sea ice in recent Arctic temperature amplification, Nature, 464, 1334–1337, https://doi.org/10.1038/nature09051, 2010.

Sellar, A. A., Jones, C. G., Mulcahy, J. P., Tang, Y., Yool, A., Wiltshire, A., O'Connor, F. M., Stringer, M., Hill, R., Palmieri, J., Woodward, S., de Mora, L., Kuhlbrodt, T., Rumbold, S. T., Kelley, D. I., Ellis, R., Johnson, C. E., Walton, J., Abraham, N. L., Andrews, M. B., Andrews,

https://doi.org/10.5194/egusphere-2026-4032
Preprint. Discussion started: 28 August 2026

T., Archibald, A. T., Berthou, S., Burke, E., Blockley, E., Carslaw, K., Dalvi, M., Edwards, J., Folberth, G. A., Gedney, N., Griffiths, P. T., Harper, A. B., Hendry, M. A., Hewitt, A. J., Johnson, B., Jones, A., Jones, C. D., Keeble, J., Liddicoat, S., Morgenstern, O., Parker, R. J., Predoi, V., Robertson, E., Siahaan, A., Smith, R. S., Swaminathan, R., Woodhouse, M. T., Zeng, G., and Zerroukat, M.: UKESM1: Description and evaluation of the U.K. Earth System Model, J. Adv. Model. Earth Syst., 11, 4513–4558, https://doi.org/10.1029/2019MS001739, 2019.

Servettaz, A. P. M., Orsi, A. J., Curran, M. A. J., Moy, A. D., Landais, A., McConnell, J. R., Popp, T. J., Le Meur, E., Faïn, X., and Chappellaz, J.: A 2000-year temperature reconstruction on the East Antarctic plateau from argon–nitrogen and water stable isotopes in the Aurora Basin North ice core, Clim. Past, 19, 1125–1152, https://doi.org/10.5194/cp-19-1125-2023, 2023.

Shu, Q., Wang, Q., Årthun, M., Wang, S., Song, Z., Zhang, M., and Qiao, F.: Arctic Ocean Amplification in a warming climate in CMIP6 models, Sci. Adv., 8, eabn9755, https://doi.org/10.1126/sciadv.abn9755, 2022.

Singh, H. A., Rasch, P. J., and Rose, B. E. J.: Increased ocean heat convergence into the high latitudes with CO_2 doubling enhances polar-amplified warming, Geophys. Res. Lett., 44, 10 583–10 591, https://doi.org/10.1002/2017GL074561, 2017.

Smith, D. M., Screen, J. A., Deser, C., Cohen, J., Fyfe, J. C., García-Serrano, J., Jung, T., Kattsov, V., Matei, D., Msadek, R., Peings, Y., Sigmond, M., Ukita, J., Yoon, J.-H., and Zhang, X.: The Polar Amplification Model Intercomparison Project (PAMIP) contribution to CMIP6: Investigating the causes and consequences of polar amplification, Geosci. Model Dev., 12, 1139–1164, https://doi.org/10.5194/gmd-12-1139-2019, 2019.

Spearman, C.: The proof and measurement of association between two things, The American Journal of Psychology, 15, 72–101, https://doi.org/10.2307/1412159, 1904.

Stuecker, M. F., Bitz, C. M., Armour, K. C., Proistosescu, C., Kang, S. M., Xie, S.-P., Kim, D., McGregor, S., Zhang, W., Zhao, S., Cai, W., Dong, Y., and Jin, F.-F.: Polar amplification dominated by local forcing and feedbacks, Nat. Clim. Change, 8, 1076–1081, https://doi.org/10.1038/s41558-018-0339-y, 2018.

Stull, R. B.: An Introduction to Boundary Layer Meteorology, vol. 13 of *Atmospheric and Oceanographic Sciences Library*, Springer Dordrecht, 1 edn., https://doi.org/10.1007/978-94-009-3027-8, 1988.

Stull, R. B.: Practical Meteorology: An Algebra-based Survey of Atmospheric Science, University of British Columbia, v1.02b edn., ISBN 978-0-88865-283-6, 2017.

Sun, K., Hu, Y., Lakhanpal, G., and Zhou, R. Z.: Spatial cross-validation for GeoAI, in: Handbook of Geospatial Artificial Intelligence, edited by: Gao, S., Hu, Y., and Li, W., CRC Press, 1 edn., 201–214, https://doi.org/10.1201/9781003308423-10, 2023.

Swain, B., Vountas, M., Singh, A., Panda, U., Song, R., Anchan, N. L., Malasani, C. R., Mallick, D., Alawode, R., Deroubaix, A., Lelli, L., Schmale, J., Tandon, A., Gunthe, S. S., Wendisch, M., Hari, V., and Bösch, H.: Contrasting anthropogenic drivers behind asymmetric warming in the Arctic and Antarctica, Ocean-Land-Atmos. Res., 5, 0127, https://doi.org/10.34133/olar.0127, 2026.

Taylor, P. C., Cai, M., Hu, A., Meehl, J., Washington, W., and Zhang, G. J.: A decomposition of feedback contributions to polar warming amplification, J. Clim., 26, 7023–7043, https://doi.org/10.1175/JCLI-D-12-00696.1, 2013.

Vallejos, R., Osorio, F., and Bevilacqua, M.: Spatial relationships between two georeferenced variables: With applications in R, Springer Cham, 1 edn., https://doi.org/10.1007/978-3-030-56681-4, 2020.

van den Broeke, M. R. and van Lipzig, N. P. M.: Factors controlling the near-surface wind field in Antarctica, Mon. Weather Rev., 131, 733–743, https://doi.org/10.1175/1520-0493(2003)131<0733:FCTNSW>2.0.CO;2, 2003.

van Lipzig, N. P. M., van Meijgaard, E., and Oerlemans, J.: The effect of temporal variations in the surface mass balance and temperature-inversion strength on the interpretation of ice-core signals, J. Glaciol., 48, 611–621, https://doi.org/10.3189/172756502781831106, 2002.

https://doi.org/10.5194/egusphere-2026-4032
Preprint. Discussion started: 28 August 2026

Voldoire, A., Saint-Martin, D., Sénési, S., Decharme, B., Alias, A., Chevallier, M., Colin, J., Guérémy, J.-F., Michou, M., Moine, M.-P., Nabat, P., Roehrig, R., Salas y Mélia, D., Séférian, R., Valcke, S., Beau, I., Belamari, S., Berthet, S., Cassou, C., Cattiaux, J., Deshayes, J., Douville, H., Ethé, C., Franchistéguy, L., Geoffroy, O., Lévy, C., Madec, G., Meurdesoif, Y., Msadek, R., Ribes, A., Sanchez-Gomez, E., Terray, L., and Waldman, R.: Evaluation of CMIP6 DECK experiments with CNRM-CM6-1, J. Adv. Model. Earth Syst., 11, 2177–2213, https://doi.org/10.1029/2019MS001683, 2019.

Wetherald, R. T. and Manabe, S.: Cloud feedback processes in a general circulation model, J. Atmos. Sci., 45, 1397–1416, https://doi.org/10.1175/1520-0469(1988)045<1397:CFPIAG>2.0.CO;2, 1988.

Williams, R. S., Marshall, G. J., Levine, X., Graff, L. S., Handorf, D., Johnston, N. M., Karpechko, A. Y., Orr, A., van de Berg, W. J., Wijngaard, R. R., and Mooney, P. A.: Future Antarctic climate: Storylines of midlatitude jet strengthening and shift emergent from CMIP6, J. Clim., 37, 2157–2178, https://doi.org/10.1175/JCLI-D-23-0122.1, 2024.

Xie, A., Zhu, J., Kang, S., Qin, X., Xu, B., and Wang, Y.: Polar amplification comparison among Earth's three poles under different socioeconomic scenarios from CMIP6 surface air temperature, Sci. Rep., 12, 16548, https://doi.org/10.1038/s41598-022-21060-3, 2022.

Yang, D., Ding, M., Zou, X., van den Broeke, M. R., van Tiggelen, M., Allison, I., Tian, B., Chen, X., and Xiao, C.: Surface energy balance and temperature inversion at Dome Argus, the summit of the East Antarctic Ice Sheet, J. Geophys. Res.: Atmos., 130, e2025JD044304, https://doi.org/10.1029/2025JD044304, 2025.

Zhang, L., Ding, M., Dou, T., Huang, Y., Lv, J., and Xiao, C.: The shallowing surface temperature inversions in the Arctic, J. Clim., 34, 4159–4168, https://doi.org/10.1175/JCLI-D-20-0621.1, 2021.

Zhang, Y., Seidel, D. J., Golaz, J.-C., Deser, C., and Tomas, R. A.: Climatological characteristics of Arctic and Antarctic surface-based inversions, J. Clim., 24, 5167–5186, https://doi.org/10.1175/2011JCLI4004.1, 2011.